Desroches, M. F., Krauskopf, B., & Osinga, H. M. (2007). The geometry of slow manifolds near a folded node.

THE GEOMETRY OF SLOW MANIFOLDS NEAR A FOLDED NODE

M. DESROCHES[*], B. KRAUSKOPF[*], H.M. OSINGA[*]

Abstract.
This paper is concerned with the geometry of slow manifolds of a dynamical system with two slow and one fast variable. Specifically, we study the dynamics near a folded node singularity, which is known to give rise to so-called canard solutions. Geometrically, canards are intersection curves of two-dimensional attracting and repelling slow manifolds, and they are a key element of slow-fast dynamics. For example, canard solutions are associated with mixed-mode oscillations, where they organize regions with different numbers of small oscillations.

We perform a numerical study of the geometry of two-dimensional slow manifolds in the normal form of a folded node in $\mathbb{R}^3$. Namely, we view the part of a slow manifold that is of interest as a one-parameter family of orbit segments up to a suitable cross-section. Hence, it is the solution of a two-point boundary value problem, which we solve by numerical continuation with the package AUTO. The computed family of orbit segments is used to obtain a mesh representation of the manifold as a surface. With this approach we show how the attracting and repelling slow manifolds change in dependence on the eigenvalue ratio μ of the reduced flow. At $\mu = 1$ two primary canards bifurcate and secondary canards are created at odd integer values of μ. We compute 24 secondary canards to investigate how they spiral more and more around one of the primary canards. The first twelve secondary canards are continued in μ to obtain a numerical bifurcation diagram.

Key words. singular perturbations, canard solution, boundary value problem, slow-fast systems, invariant manifolds

AMS subject classifications. 34E15, 34C30, 37C10, 65L10

1. Introduction. Multiple time scale systems are characterized by the property that certain variables evolve on vastly different time scales, which means that the systems may display dynamics that is composed of slow and fast elements. The occurence of different time scales is quite natural in many applications, including chemical reaction dynamics [9, 32, 34, 36, 38], cell modelling [14, 42, 43], electronic circuits [12, 46, 47], and laser dynamics [15, 20]. The first example of slow-fast dynamics was discovered by Van der Pol [46, 47] in the 1920s. He considered an electrical circuit with a triode valve where the current is a cubic function of the voltage. The mathematical model of this circuit — known today as the Van der Pol equations — has the form of a planar vector field model of an oscillator with a cubic nonlinear damping term. The Van der Pol equations show sustained oscillations, which are harmonic for small damping parameter but very non-harmonic when the damping parameter is large. In the latter case the periodic solution is composed of slow motion that closely follows attracting segments of the underlying cubic curve (which forms one of the nullclines), followed by fast jumps as the trajectory reaches either of the two folds of this curve. At the jumps one of the variables barely changes until the trajectory reaches another attracting segment of cubic curve. Van der Pol called these periodic solutions *relaxation oscillations*. Models showing relaxation oscillations quite similar to that of the Van der Pol equations have been found in other application areas. A well known example is the FitzHugh-Nagumo system, which also has two time scales and a cubic nonlinearity. It was derived independentely by FitzHugh [23] and Nagumo [37] as a simplified planar version of the famous Hodgkin-Huxley equations for the action potential of the giant axon of a squid in terms of transmembrane currents [30].

At the end of the 1970s, Benoît *et al.* [5] found and analyzed even more unusual periodic solutions in the Van der Pol system, which they called *canards*. A canard orbit has the spe-

[*]Department of Engineering Mathematics, University of Bristol, Bristol BS8 1TR, United Kingdom.
The authors thank John Guckenheimer and Martin Wechselberger for helpful discussions. M.D. was supported by grant EP/C54403X/1 from the Engineering and Physical Sciences Research Council (EPSRC), and H.M.O. by an EPSRC Advanced Research Fellowship grant.

cial property that it follows at least one unstable segment of the underlying cubic nullcline. In other words, the trajectory does not jump at the respective fold. Canard orbits account for a sudden increase in the amplitude of the attracting periodic orbit in the transition from harmonic oscillations to relaxation oscillations. This change is known as a *canard explosion*, and it occurs in an exponentially small interval of the damping parameter. For this reason, the associated canards are extremely difficult to observe in two-dimensional slow-fast systems.

The situation is very different in three-dimensional slow-fast systems, where canards may occur in much larger regions of system parameters. They have been found in numerous slow-fast systems. For example, canards explain sudden changes in amplitude and period of oscillatory behavior in chemical reactions [9, 32, 34, 36, 38]; they organize the dynamics in models of coupled neurons and also play an important role in intracellular activities [14, 42, 43]; canards have been studied for their role in diffusion-induced instabilities [9, 40]; and Guckenheimer *et al.* [6, 28] recently performed an extensive study of a reduced hybrid model of the forced Van der Pol system, which revealed relaxation oscillations and canard orbits of different types. A related phenomenon in slow-fast systems are *mixed-mode oscillations*, which consists of large-amplitude excursions followed by small-amplitude motions that are typically of (relatively) high frequency. This type of oscillations have been found in chemical and biological systems, and the connection between mixed-mode oscillations and canards has been clarified recently [8, 34, 43, 48]; see also the special issue [7].

For the theoretical study of canards in three-dimensional phase space one considers a dynamical system with two slow and one fast variable of the form

$$\left\{ \begin{array}{rcl} \dot{u}_1 & = & g_1(u_1, u_2, v, \varepsilon), \\ \dot{u}_2 & = & g_2(u_1, u_2, v, \varepsilon), \\ \varepsilon \dot{v} & = & f(u_1, u_2, v, \varepsilon). \end{array} \right. \tag{1.1}$$

Here g_1, g_2, and f are sufficiently smooth functions, and $\varepsilon > 0$ is a small parameter that separates the different time scales. Since ε is small, the variables u_1 and u_2 move on a slower time scale than the fast variable v. The equivalent of the cubic nullcline of the Van der Pol equations is now the surface — called the *critical manifold* – that is given as the v-nullcline of (1.1). The critical manifold has repelling parts and attracting parts, which meet along one-dimensional fold curves. As for the Van der Pol equations, the slow dynamics takes place close to the critical manifold. When a fold is reached two things can happen. The trajectory may jump at the fold curve towards another attracting sheet of the critical manifold. If a global return mechanism is present, e.g., the critical manifold is S-shaped with two fold curves, such jumps give rise to classical relaxation oscillations [35, 45]. The other possibility is that the trajectory is a canard solution that does not jump at the fold curve, but instead stays near the repelling part of the critical manifold for a certain amount of time.

Since the beginning of the 1980s, when canard solutions were first discovered, different analytical techniques have been applied to their study. Initially, non-standard analysis [3, 4, 5] and matched asymptotic expansions [35, 18] were used, but more recently canards have been studied with tools from geometric simgular perturbation theory [22, 31]. Underlying this geometric approach is the realization that the study of canard solutions comes down to understanding the dynamics of the system near folds of the critical manifold. Of specific interest here are (isolated) points on fold curves where the direction of flow changes from pointing towards the fold to pointing away from the fold. These points, called *folded singularities*, are key to the understanding of canard solutions.

We are concerned here with the case of a *folded node*, which is a type of folded singularity that has been identified as an organizing center for the creation of canard solutions. Figure 1 shows the dynamics for $\varepsilon = 0$ near a folded node on a regular fold curve F along

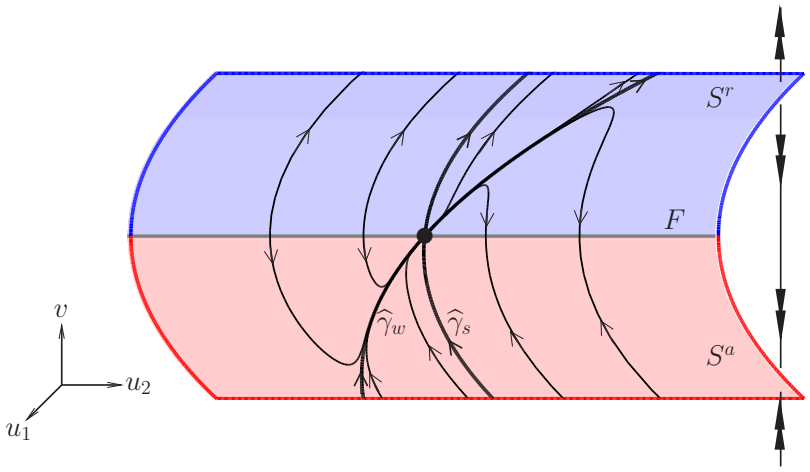

FIG. 1. *Sketch of a folded critical manifold S consisting of an attracting sheet S^a and a repelling sheet S^r that meet at a fold curve F. The sketched flow on S is the generic slow flow near a folded node (black dot); shown are two singular canards $\widehat{\gamma}_s$ and $\widehat{\gamma}_w$ and some other trajectories of the slow flow. The action of the fast flow is shown along one fast fiber.*

which the attracting sheet S^a and the repelling sheet S^r of the critical manifold join. At the folded node (black dot), the direction of the flow on the critical manifold changes. This allows for the existence of canard solutions on the critical manifold that cross F at the folded singularity with nonzero speed and then follow the repelling sheet S^r. These canards for $\varepsilon = 0$, which are referred to as *singular canards*, occur in an entire region that is bounded by the repelling part of the fold curve F and the special canard solution $\widehat{\gamma}_s$ in Fig. 1. The main question is now what can be said about the dynamics near a folded node when $\varepsilon \neq 0$. According to a well-known result by Fenichel [21, 22], away from the fold curve F the attracting and repelling sheets give rise for $\varepsilon \neq 0$ to an *attracting slow manifold* S^a_ε and a *repelling slow manifold* S^r_ε, respectively. Importantly, the two surfaces S^a_ε and S^r_ε do not connect along the fold curve for $\varepsilon \neq 0$, but rather intersect, generically transversely, in one-dimensional solution curves. Hence, these curves are referred to as *maximal canards*, as they stay close to the repelling part of the critical manifold for a certain amount of time. In other words, finding the structure of canard solutions near the folded node is equivalent to understanding the geometry of the two-dimensional surfaces S^a_ε and S^r_ε.

Canards near a folded node are best analyzed in a normal form setting. Normal forms for all types of folded singularities, including the folded node, were derived by Il′yashenko [2, part I, chapter 4]. Benoît [4] completely analyzed the case of a folded saddle and also considered the case of a folded node. He proved the existence of two maximal canards under a non-resonance condition with tools of nonstandard analyis and found secondary canards with spiralling behavior by numerical integration. Szmolyan and Wechselberger [44] consider all cases of folded singularities. For the folded node they proved the existence of primary canards by using geometric singular perturbation theory in combination with blow-up transformations. Guckenheimer and Haiduc [27] proved that there are infinite many secondary canards near a folded node. Wechselberger [48] studied how secondary canards bifurcate

from the weak primary canard and he sketched the underlying bifurcation structure. Both Guckenheimer and Haiduc [27] and Wechselberger [48] find canards numerically by computing the one-dimensional intersection curves of the attracting and repelling slow manifolds in a two-dimensional cross section with a shooting approach (integration from a line of initial conditions far from the fold curve); the canards are then identified as crossings of the two curves.

Our goal is to compute and visualize the slow manifolds as surfaces and the canards as trajectories in $\mathbb{R}^3$ to obtain additional geometric insight into the dynamics near a folded node. To this end, we consider the normal form as used in [48], which is given as the three-dimensional vector field

$$\left\{ \begin{array}{rcl} \dot{x} & = & \frac{1}{2}\mu y - (\mu+1)z, \\ \dot{y} & = & 1, \\ \dot{z} & = & x + z^2. \end{array} \right. \tag{1.2}$$

In (1.2) the folded node is at the origin and the parameter μ is the ratio of the eigenvalues of the Jacobian matrix of the so-called desingularized reduced flow evaluated at the folded node. Note that, as a result of a parameter dependent blow-up procedure, (1.2) does not depend on ε. Nevertheless, this normal form describes how the attracting and repelling slow manifolds intersect near a folded node. Specifically, for any μ (1.2) has an attracting slow manifold C^- and a repelling slow manifold C^+ that intersect in the maximal canards one wants to study; see Sec. 2 for more information on the derivation and meaning of the normal form.

Specifically, we compute in this paper the slow manifolds C^- and C^+ of (1.2) as surfaces in $\mathbb{R}^3$. This is achieved by representing a piece of interest of a slow manifold as a one-parameter family of orbit segments that satisfy suitably chosen boundary conditions. The resulting boundary value problem is solved with the continuation and collocation routines of the package AUTO [13]. This setup is very flexible and accurate, because it is based on the continuation of two-point boundary value problems [33]. It allows us to adjust the boundary conditions to emphasize certain local features of the underlying dynamics in the vicinity of the folded node. In particular, we are able to compute the slow manifolds past the folded node and show their exponential growth on the other side of it. Our method allows for a very precise visualization of the behavior of the slow manifolds in the vicinity of the folded node. In particular, we are able to capture in detail the complexity of their intersections, that is, the canards. For increasing μ, the two surfaces rotate more and more around the weak primary canard (the perturbation of $\widehat{\gamma}_w$ in Fig. 1), which leads to the creation of secondary canards at odd integer values of μ. Our method allows us to detect canards and to continue them as solutions of a boundary value problem in the parameter μ. We compute up to 24 secondary canards and show how they spiral around the weak primary canard. Furthermore, we continue 12 secondary canards in μ to obtain a numerical bifurcation diagram.

Note that very few attempts have been made so far to produce accurate computations of slow manifolds as surfaces. Milik *et al.* [34] visualize slow manifolds in the normal form of a folded saddle-node; in this special case (of codimension one) the system decouples into a one-parameter family of two-dimensional systems, so that the slow manifolds can be built up from individual one-dimensional stable and unstable manifolds (which can be found by integration). Ginoux and Rossetto [24, 25] derive an implicit equation of a two-dimensional slow manifold as the locus where the torsion vanishes. The implicit equation is then solved numerically to obtain a grid approximation of a part of the manifold under consideration; their examples include folded slow manifolds in Chua's circuit model [24] and in the Hindmarsh-Rose model of a bursting neuron [24]. Both methods are quite different from our approach. Our boundary value problem formulation not only allows to compute slow manifolds as global objects in a specified region of interest, but also to detect canards

and follow them in system parameters. More generally, computing invariant manifolds by continuation and collocation as solution families subject to suitable boundary conditions is a very flexible method [33], which is particularly well suited for slow-fast systems [19]. Our method is not restricted to the normal form setting but can be used more widely, for example, for the study of canards in the self-coupled FitzHugh-Nagumo system [10].

The outline of this paper is as follows. In the next section we present some technical background material. We briefly review slow-fast systems in Sec. 2.1, explain the blow-up method in Sec. 2.2, and then discuss some known properties of the normal form (1.2) in Sec. 2.3. Section 3 explains in detail how to compute slow manifolds as collections of orbit segments. In Sec. 4 we show how the slow manifolds change with μ, and Sec. 5 is devoted to the detection and continuation of the secondary canards. In Sec. 6 we show that the geometry of the slow manifolds does not change topologically when the normal form is perturbed. We conclude with a summary and outlook in Sec. 7.

2. Background on the folded node. In this section we recall some basic facts about singularly perturbed dynamical systems, folded singularities and the blow-up method to analyze them. We consider the three-dimensional normal form (1.2), as studied, for example, by Benoît [3, 4], Guckenheimer and Haiduc [27], and Wechselberger [48]. Following [48] we show how the normal form is derived from a generic three-dimensional system with a folded node at the origin and present some useful properties of (1.2).

2.1. Slow-fast dynamical systems. The *slow-time system* (1.1) defines a vector field using the slow time t. An alternative way of writing (1.1) is to introduce the fast time $\tau = \frac{t}{\varepsilon}$, which gives the *fast-time system*

$$\left\{ \begin{array}{rcl} u_1' &=& \varepsilon g_1(u_1, u_2, v, \varepsilon), \\ u_2' &=& \varepsilon g_2(u_1, u_2, v, \varepsilon), \\ v' &=& f(u_1, u_2, v, \varepsilon), \end{array} \right. \tag{2.1}$$

where the prime indicates the derivative with respect to the fast time τ. This rescaling of time is valid only for $\varepsilon \neq 0$ and does not modify the geometry of the trajectories. The main question is whether it is possible to understand the dynamics for small $\varepsilon > 0$ by considering the two limits of (1.1) and (2.1) given by $\varepsilon = 0$.

The limit of the slow-time system (1.1) for $\varepsilon = 0$ is known as the *reduced system* or *slow subsystem*

$$\left\{ \begin{array}{rcl} \dot{u}_1 &=& g_1(u_1, u_2, v, 0), \\ \dot{u}_2 &=& g_2(u_1, u_2, v, 0), \\ 0 &=& f(u_1, u_2, v, 0). \end{array} \right. \tag{2.2}$$

System (2.2) is a set of differential algebraic equations (DAE) on the slow time scale, namely, two differential equations constrained by the algebraic equation $f = 0$. This condition defines the *critical manifold*

$$S := \left\{ (u_1, u_2, v) \in \mathbb{R}^3 \mid f(u_1, u_2, v, 0) = 0 \right\}, \tag{2.3}$$

on which the dynamics of the reduced system (2.2) takes place. We obtain differential equations that describe the flow of the reduced system (2.2) on S as follows. Differentiating the algebraic equation $f = 0$ with respect to time yields

$$\left\{ \begin{array}{rcl} \dot{u}_1 &=& g_1(u_1, u_2, v, 0), \\ \dot{u}_2 &=& g_2(u_1, u_2, v, 0), \\ -f_v \dot{v} &=& f_{u_1} \dot{u}_1 + f_{u_2} \dot{u}_2. \end{array} \right. \tag{2.4}$$

We then rescale (2.4) by $-f_v$ to obtain the vector field

$$\left\{\begin{array}{rcl} \dot{u}_1 &=& -f_v g_1(u_1,u_2,v,0),\\ \dot{u}_2 &=& -f_v g_2(u_1,u_2,v,0),\\ \dot{v} &=& f_{u_1} g_1 + f_{u_2} g_2, \end{array}\right. \tag{2.5}$$

that generates a *slow flow* on S.

The limit of the fast-time system (2.1) for $\varepsilon = 0$ is known as the *layer system* or *fast subsystem*

$$\left\{\begin{array}{rcl} u_1' &=& 0,\\ u_2' &=& 0,\\ v' &=& f(u_1,u_2,v,0). \end{array}\right. \tag{2.6}$$

The variables u_1 and u_2 are constants in system (2.6) and enter the equation for v as parameters. Hence, the layer system is a two-parameter family of differential equations on the fast time scale. The critical manifold S plays a key role in the layer system as well, namely, as a manifold of equilibria.

The idea of geometric singular perturbation theory [22, 31] is to understand the dynamics of system (1.1) with $\varepsilon > 0$ sufficiently small by splitting the motion into its fast and slow components. The fast dynamics of (1.1) is described by the layer system (2.6), meaning that trajectories behave like solutions of (2.6) until they get close to S. On the slow time scale, solutions are well approximated by the reduced system (2.2); in particular, trajectories remain confined to an ε-neighborhood of S. The overall dynamics can indeed be understood in this way if the critical manifold S is *normally hyperbolic*. This means that the dynamics in the normal direction to the manifold dominates the dynamics in the tangent direction [29]. Due to results by Fenichel [21, 22], a normally hyperbolic critical manifold S persists under small perturbations as a nearby normally hyperbolic invariant manifold S_ε for the singularly perturbed system (1.1).

In the vicinity of points where normal hyperbolicity fails, the singularly perturbed problem can give rise to very complex dynamics. In order to study what happens when S is not normally hyperbolic, we consider the projection of S onto the (u_1,u_2)-plane of slow variables. The critical manifold S consists of regular points where $f_v \neq 0$ and critical points of the projection where $f_v = 0$. According to singularity theory [1], regular points are generic and they correspond to points where S is normally hyperbolic. Moreover, a generic critical point is a fold point, and together the fold points form a codimension-one submanifold F of S. Along F two sheets of S meet. In $\mathbb{R}^3$ there may be cusp points (degenerate folds), but they are generically isolated. We focus here on fold points and their influence on the dynamics of system (1.1).

Specifically, we consider a critical manifold S with (locally) a nonempty fold curve that does not contain cusp points. Therefore, S can be written as $S = S^a \cup F \cup S^r$, where S^a and S^r refer to the attracting and repelling sheets of S, respectively, that meet at F; formally

$$\begin{array}{rcl} S^a &=& \{(u_1,u_2,v) \in S \mid f_v(u_1,u_2,v) < 0\},\\ F &=& \{(u_1,u_2,v) \in S \mid f_v(u_1,u_2,v) = 0\},\\ S^r &=& \{(u_1,u_2,v) \in S \mid f_v(u_1,u_2,v) > 0\}. \end{array} \tag{2.7}$$

System (2.4) is singular along F while the desingularized system (2.5) governs the dynamics in the vicinity of the critical manifold S. Note that the rescaling by $-f_v$ that achieves this desingularization changes the direction of time where $f_v > 0$, that is, on the repelling sheet S^r of the critical manifold S.

Roughly speaking, the original system (1.1) is governed by system (2.5) when it evolves almost on the attracting sheet S^a. The situation changes when a trajectory reaches the fold curve F, that is, when f_v becomes zero. In the generic situation, that is, if $\dot{v} \neq 0$ the prominent dynamics switches to the fast dynamics (2.6) and the trajectory escapes from S along a fast fiber parallel to the v-axis. The condition $\dot{v} = f_{u_1} g_1 + f_{u_2} v_2 \neq 0$ is called the *normal switching condition* [35] and means geometrically that the reduced flow projected onto the (u_1, u_2)-plane is not tangent to the fold curve F. The point on the fold curve F where the change of dynamics occurs is called a *jump point*. If S is S-shaped, that is, there are two separate attracting sheets and two fold curves connected to a repelling sheet, then the presence of jump points typically leads to the existence of *relaxation oscillations* [35, 45], that is, periodic solutions that involve both fast and slow segments; a detailed discussion of this phenomenon is given in [28] for the forced Van der Pol system.

If $f_{u_1} g_1 + f_{u_2} v_2 = 0$ then (2.5) has an equilibrium on the fold curve F and there is no jump. Such an equilibrium is called a *folded singularity*. According to the topological type of the singularity as an equilibrium of system (2.6), one has generically *folded nodes*, *folded saddles*, and *folded foci*. Locally, the dynamics near a folded singularity can be described by normal forms. Normal forms for planar or three-dimensional slow-fast systems were first derived by Il′yashenko [2]. These normal forms were subsequently used by Benoît [4], Szmolyan and Wechselberger [44], and Guckenheimer and Haiduc [27], among others, to obtain analytical results concerning the possible bifurcations near such folded singularities.

The case of a folded-node singularity is sketched in Fig. 1 and several trajectories of the slow flow associated with the normal form (1.2) are shown. Notice the change of direction of the slow flow across the fold curve F. As a result, some initial conditions on S^a are attracted to regular points on F, which leads to a jump. However, an entire wedge exists, bounded by the singular canard $\widehat{\gamma}_s$ and a half-line on F that ends at the folded node, where trajectories converge to the folded node and pass through to follow the repelling sheet S^r. This wedge is called the *funnel region* [48] and it is responsible for the generic existence of canard solutions in systems with $\varepsilon \neq 0$. Note that Fenichel theory cannot be invoked to describe the geometry of the slow manifolds in this region of the phase space simply by using the unperturbed limiting problems (2.2) and (2.6). Instead, blow-up methods are used to obtain the dynamics through the funnel region.

2.2. Blow-up of the folded node. One can apply the method of blow-up in the setting of geometric singular perturbation theory [16, 41]. The general idea is to rescale the variables of the original problem together with the singular parameter ε. In this way, one can transform a singularly perturbed system into a regularly perturbed system that is defined on a higher-dimensional phase space.

The slow manifolds S^a_ε and S^r_ε correspond to ε-leaves of three-dimensional attracting and repelling center manifolds M_a and M_r of the extended system

$$\left\{ \begin{array}{rcl} u_1' &=& \varepsilon g_1(u_1, u_2, v, \varepsilon), \\ u_2' &=& \varepsilon g_2(u_1, u_2, v, \varepsilon), \\ v' &=& f(u_1, u_2, v, \varepsilon), \\ \varepsilon' &=& 0. \end{array} \right. \tag{2.8}$$

The linearization of the extended system (2.8) has all eigenvalues equal to zero at the folded node. Hence, one cannot apply center manifold theory at points on F and describe the behavior of the slow manifolds in a neighborhood of F. A good way of overcoming this difficulty is to apply a blow-up transformation at the folded node, which is a degenerate singularity of system (2.8). Roughly speaking, the blow-up method is a well-chosen coordinate transformation that desingularizes such a degenerate singularity. It was originally developed for planar

vector fields [17], but has been adapted to the case of three-dimensional singularly perturbed systems [44, 48]. The change of coordinates transforms the degenerate singularity at the origin into a sphere $\mathbb{S}^3$ that contains points with (at least) one non-zero eigenvalue. Then the general methods of dynamical systems are applicable, in particular, center manifold theory; see [44] for a detailed exposition of the blow-up in this specific context.

In the case of a three-dimensional singularly perturbed system with a folded node at the origin, the desingularizing transformation is defined by

$$u_1 = \rho^2 x,\ u_2 = \rho y,\ v = \rho z,\ \varepsilon = \rho^2 \bar{\varepsilon},$$

where $(x, y, z, \bar{\varepsilon}) \in \mathbb{S}^3$ and $\rho \in [0, \rho_0]$ is a new radial parameter. As is explained in [48], two charts κ_1 and κ_2 of the sphere $\mathbb{S}^3$ suffice to understand the entire extended phase space. These charts yield so-called *directional rescalings* obtained by setting one coordinate in $\mathbb{S}^3$ equal to ± 1 and desingularizing the vector field in both charts, where chart κ_1 is defined by $x = -1$ and chart κ_2 by $\bar{\varepsilon} = 1$.

To investigate the possible intersections between the slow manifolds, that is, the existence of maximal canards, one only needs to look at chart κ_2, which describes the situation on the blown-up locus. As a main result, the blow-up extends the normal hyperbolicity of the slow manifolds S^a_ε and S^r_ε to the blown-up sphere. After desingularization, the system in κ_2 is given by

$$\left\{ \begin{array}{rcl} \dot{x} &=& \frac{1}{2}\mu y - (\mu+1)z + O(\rho), \\ \dot{y} &=& 1, \\ \dot{z} &=& x + z^2 + O(\rho). \end{array} \right. \tag{2.9}$$

By definition of the directional rescaling in chart κ_2 we have $\rho = \sqrt{\varepsilon}$. The key idea is now to study system (2.9) for $\rho = 0$, which is the normal form (1.2).

We now explain briefly why it is sufficient to consider system (1.2) to obtain all the information concerning the original singularly perturbed system (1.1). To avoid technical details about the blow-up, which can be found in [44, 48], we follow here the intuitive point of view (and the underlying notations) developed in [8]. By Fenichel's theorems, for any fixed $\varepsilon > 0$ sufficiently small, the slow manifolds S^a_ε and S^r_ε exist outside a neighborhood of the fold curve F, that is, for $u_1 < -\delta$ (where $\delta > 0$ depends on ε). It is possible to extend S^a_ε and S^r_ε up to section $\sigma' := \{u_1 = -\delta'\varepsilon\}$ ($\delta' > 0$ such that $-\delta < -\delta'\varepsilon$) by considering orbit segments starting in section $\sigma := \{u_1 = -\delta\}$ and ending in section σ'. Note that these cross-sections are well defined as long as the flow is not tangent to the u_2-axis, which is satisfied in the vicinity of a folded node. Hence, σ and σ' are defined on intervals I_{u_2} and I'_{u_2} of u_2, respectively. Then we define, still following [8], the sets S^a_ρ and S^r_ρ as collections of orbit segments starting in I_{u_2} and ending in I'_{u_2}. One can prove [48] that S^a_ρ and S^r_ρ are smooth perturbations of the critical manifold S outside a neighborhood of the fold curve F of size $(O(\varepsilon), O(\rho), O(\varepsilon))$ in (u_1, u_2, v). The great benefit of the blow-up transformation in chart κ_2 is that for $\rho \to 0$ the slow manifolds S^a_ρ and S^r_ρ tend to invariant sets C^- and C^+ of (1.2), respectively. This is possible because in (x, y, z), the section σ is given by $x = -\delta/\varepsilon$, hence by $x = -\delta/\rho^2$, and σ' by $x = -\delta'$. Therefore, S^r_ρ and S^a_ρ can be seen as smooth $O(\rho)$ perturbations of C^+ and C^-, respectively.

In other words, we can study and understand the dynamics of $C^\pm$ up to the folded node; in particular, we can investigate their transverse intersections and deduce information about the singularly perturbed system. Indeed, by the Implicit Function Theorem, transverse intersections of C^- and C^+ persist under small perturbations $\rho > 0$, as system (2.9) is a regularly perturbed system with respect to ρ. Consequently, the geometry of the manifolds $C^\pm$, which

we refer to as the repelling and attracting slow manifolds from now on, contains all the relevant information regarding the corresponding "true" slow manifolds S^r_ε and S^a_ε of system (1.1), respectively. Indeed, the study of the geometry of $C^\pm$ is the main topic of this paper.

2.3. Properties of the normal form. The normal form (1.2) was already studied, in an equivalent form, by Benoît in [4] and Guckenheimer and Haiduc in [27]. By looking at the equation for $\dot{z}$ in (1.2), it is clear that the critical manifold associated with this normal form is the parabolic cylinder

$$S := \{(x, y, z) \in \mathbb{R}^3 \mid x + z^2 = 0\}, \tag{2.10}$$

that is folded along the y-axis, that is,

$$F := \{(0, y, 0) \in \mathbb{R}^3\}. \tag{2.11}$$

This is exactly the picture in Fig. 1. An important property of the normal form (1.2) is its invariance under the time-reversing symmetry $(x, y, z, t) \mapsto (x, -y, -z, -t)$. Therefore, it suffices to concentrate on the attracting slow manifold C^-; the repelling slow manifold C^+ is given by the symmetry. A main advantage of (1.2) is that it possesses two explicit canard solutions of algebraic growth, γ_s and γ_w, given as

$$\begin{aligned} \gamma_s(t) &= \left(-\frac{\mu^2}{4}t^2 + \frac{\mu}{2},\ t,\ \frac{\mu}{2}t\right), \\ \gamma_w(t) &= \left(\ -\frac{1}{4}t^2 + \frac{1}{2},\ t,\ \frac{1}{2}t\right). \end{aligned} \tag{2.12}$$

We refer to γ_s as the *strong canard* and to γ_w as the *weak canard*, because they correspond to the strong and the weak eigendirection of the linearization of system (1.2) at the folded node, respectively. Note that the geometry of the critical manifolds for $\mu > 1$ and for $1/\mu \in [0, 1]$ is topologically the same (where the roles of γ_s and γ_w are interchanged); recall that μ denotes the ratio of the eigenvalues of system (2.5) projected onto the (y, z)-plane and linearized at the origin. Therefore, we consider here the changes of the slow manifolds $C^\pm$ as a function of μ only for $\mu \geq 1$.

It has been proved that $C^\pm$ intersect transversely along γ_s and γ_w when μ is not an integer [4, 44]. For integer values of μ the manifolds C^+ and C^- intersect transversely along γ_s and tangentially along γ_w. A new canard is created from the weak canard γ_w at every odd integer value of the parameter μ (for $\mu \geq 3$) [48]. The bifurcating canards η_i are called *secondary canards*. It was analytically proved in [44] that the slow manifolds C^- and C^+ spiral $\lfloor \mu \rfloor$ times around the weak canard γ_w (here $\lfloor q \rfloor$ denote the integer part of the real number q). Due to the time-reversing symmetry of the normal form, this implies that C^- and C^+ make $\lfloor \frac{\mu-1}{2} \rfloor$ full rotations around each other. Each one of these full rotations ends in a transverse intersection along a secondary canard. Hence, there are $\lfloor \frac{\mu-1}{2} \rfloor$ secondary canards that successively make one additional complete revolution around γ_w. More precisely, η_i makes $i + \frac{1}{2}$ rotations around γ_w; see already Sec. 5. Geometrically, we can think of the strong canard γ_s as the secondary canard η_0, because γ_s makes a half rotation around γ_w. Due to the symmetry of (1.1), the intersection points of the canard solutions with the section $\Sigma_0 = \{y = 0\}$ lie on the x-axis, and their order is such that γ_w is always located between $\eta_{\lfloor \frac{\mu-1}{2} \rfloor}$ and $\eta_{\lfloor \frac{\mu-1}{2} \rfloor - 1}$.

3. Computing slow manifolds. To get an insight into the geometry of the attracting and repelling slow manifolds $C^\pm$ we developed a computational technique for their numerical approximation and visualization. The main underlying idea of our approach is that one

can compute (a finite part of) a two-dimensional invariant manifold of a system of ordinary differential equations as a collection of orbit segments by numerical continuation of a one-parameter family of two-point boundary value problems. This idea can be applied in a wide variety of contexts [33]. Below we explain how we use this general idea to compute $C^{\pm}$ for the normal form; see [10] for details on how to compute $C^{\pm}$ for systems not in normal form.

3.1. Slow manifolds as collections of orbit segments. As is common in numerical continuation, we consider a vector field of the form

$$\dot{\mathbf{u}} = T\mathbf{g}(\mathbf{u}, \lambda), \tag{3.1}$$

where $\mathbf{g} : \mathbb{R}^n \times \mathbb{R}^p \to \mathbb{R}^n$ is sufficiently smooth and $T \in \mathbb{R}$ and $\lambda \in \mathbb{R}^p$ are parameters. The parameter T is the total integration time. It appears explicitly as a free parameter on the right-hand side of (3.1), so that an orbit segment $\mathbf{u}(t)$ is always represented over the interval $[0, 1]$. By imposing suitable boundary conditions on solutions of (3.1) we can characterize any k-dimensional invariant submanifold in $\mathbb{R}^n \times \mathbb{R}^p$. To be more precise, we consider the boundary conditions

$$\begin{cases} \mathbf{u}(0) \in L, \\ \mathbf{u}(1) \in \Sigma, \end{cases} \tag{3.2}$$

where L is a one-dimensional submanifold and Σ a codimension-one submanifold of $\mathbb{R}^n$. One needs $(n-1)$ boundary conditions to restrict $\mathbf{u}(0)$ to the curve L and one boundary condition to restrict $\mathbf{u}(1)$ to the $(n-1)$-dimensional manifold Σ. Hence, the total number of boundary conditions in (3.2) is n. That is, with T as a free parameter Eqs. (3.1)–(3.2) define a one-parameter family of well-posed two-point boundary value problems that represent orbit segments starting at L and ending in the section Σ; see, for example, [11]. The family is parametrized by the position of $\mathbf{u}(0)$ on L, and T is the integration time to reach Σ from L. Depending on the choice of L and Σ, this general setup can be used to compute different types of dynamical objects, including two-dimensional invariant manifolds [33] and their one-dimensional intersection curves with the section Σ [19].

In the present setting the phase space is three dimensional and our goal is to find appropriate definitions for L and Σ so that (3.1)–(3.2) define $C^{\pm}$ as surfaces in a region of interest. Since C^+ can be found from C^- by symmetry in (1.2), we only explain here the computation of C^-. The family of orbit segments obtained by continuation of (3.1)–(3.2) defines (part of) the two-dimensional manifold C^-, provided the one-dimensional submanifold L satisfies $L \subset C^-$ [22, 48]. Since we do not know C^-, we choose L on the attracting sheet S^a of the critical manifold S sufficiently far away from the fold curve F, that is in a region where S^a is a good approximation of C^-. Then the boundary value problem defines an approximation of C^-. From (1.2) and (2.10) we know that

$$S^a = \{(x, y, z) \in \mathbb{R}^3 \mid x + z^2 = 0,\ z < 0\}.$$

Since the fold curve F is the y-axis, we define

$$L = L^-_\xi := \{(-\xi, s, -\sqrt{\xi}) \mid s \in \mathbb{R}\}, \tag{3.3}$$

which is the line on S^a with $x = -\xi$ parallel to F at 'distance' $\xi > 0$ from F. The interesting dynamics takes place near the folded node on F, so a suitable choice for Σ is a plane transverse to F near the origin. We define

$$\Sigma = \Sigma_\alpha := \{y = \alpha\}, \tag{3.4}$$

where $\alpha \geq 0$. The two-point boundary value problem (3.1)–(3.2) for the choices (3.3) and (3.4) defines a one-parameter family of orbit segments that lie on C^- in good approximation, provided ξ is large enough.

3.2. Finding a first orbit segment on the slow manifold. To start the continuation we must provide a first orbit segment that solves (3.1) subject to the boundary conditions (3.2). For the normal form (1.2) two explicit canard solutions are known, which we can use as seed solutions. Note that neither one of the two explicit solutions has a point in common with the attracting sheet S^a of the critical manifold, which means that it is not possible to choose ξ such that the two explicit canard solutions contain segments that start on L_ξ^- and solve the boundary value problem (3.1)–(3.2). However, we only use the explicit solutions as a seed for the Newton iteration, that is, we must find a suitable solution segment such that Newton's method converges to a solution of (3.1)–(3.2).

To be concrete, we start from the strong canard γ_s given in (2.12) and consider the initial orbit segment

$$\mathbf{u}(t) = \gamma_s(tT + t_0), \qquad 0 \le t \le 1, \tag{3.5}$$

for some start time t_0 and total integration time T. We choose $t_0 < 0$ such that the x-coordinate of $\gamma_s(t_0)$ is equal to $-\xi$, that is,

$$-\frac{\mu^2}{4}t_0^2 + \frac{\mu}{2} = -\xi.$$

In order to satisfy the second boundary condition $\mathbf{u}(1) \in \Sigma_\alpha$, we need

$$\gamma_s(T + t_0) \in \Sigma_\alpha \Leftrightarrow T + t_0 = \alpha.$$

Note that the start time t_0 must be negative, because the y-coordinate acts as time in the normal form (1.2) and we wish to preserve the direction of time. Therefore, we have

$$t_0 = -\sqrt{\frac{2\mu + 4\xi}{\mu^2}} \quad \text{and} \quad T = \alpha + \sqrt{\frac{2\mu + 4\xi}{\mu^2}}. \tag{3.6}$$

The solution segment (3.5) only approximately satisfies the boundary condition $\mathbf{u}(0) \in L_\xi^-$, namely, the difference between the z-coordinates of $\mathbf{u}(0) = \gamma_s(t_0)$ and the point on L_ξ^- at $s = t_0$ is

$$\frac{\mu}{2}\sqrt{\frac{2\mu + 4\xi}{\mu^2}} - \sqrt{\xi} = \frac{\mu}{2\left(\sqrt{\frac{\mu}{2} + \xi} + \sqrt{\xi}\right)}. \tag{3.7}$$

This difference is small, provided $\xi \gg \mu$, and decreases as $\xi \to \infty$. Hence, if ξ is large enough, we expect that Newton's method converges and the first correction step of the continuation leads to a solution of (3.1)–(3.2). We remark that for a slow-fast system that is not in normal form an explicit solution is generally not known. This difficulty can be overcome with a homotopy approach, as is demonstrated in [10].

3.3. Computation of C^- from L_ξ^- to Σ_α. The computed part of C^- depends on the two user-specified parameters ξ and α that define L_ξ^- and Σ_α, respectively. The parameter ξ controls the accuracy of the computation in that it determines the initial distance between C^- and the critical manifold S^a. By construction, an orbit segment satisfying (3.1)–(3.2) converges to an actual orbit segment on C^- in the limit $\xi \to \infty$. It is a very difficult task beyond the scope of this paper to find an explicit ξ-dependent error bound for the approximation of C^- and how it depends on μ. To derive a practical measure for the accuracy of the computations presented here we make use of the fact that the strong canard γ_s is given as an explicit

solution (2.12). As mentioned in Sec. 3.2, the orbit segment (3.5) of γ_s is the seed solution for Newton's method, and we use the difference between $\gamma_s(tT+t_0)$ and the approximate solution $\mathbf{u}^*(t)$ as an indication of the overall approximation error. Namely, we consider the pointwise difference between $\gamma_s(tT+t_0)$ and $\mathbf{u}^*(t)$ with $0 \leq t \leq 1$ and ensure that it is sufficiently small. At $t=0$ this difference is given by (3.7), and it decreases exponentially for $t>0$; this decrease is particularly fast due to the difference in time scales. Specifically, we only consider the difference in the z-coordinate and require that

$$|\,\gamma_s(tT+t_0)-\mathbf{u}^*(t)\,|_z < 10^{-5}$$

for all t with $\mathbf{u}_x^*(t) > -\frac{1}{2}\xi$. In other words, this condition ensures the accuracy of the second and relevant part of the orbit segment, and we found that it is satisfied with $\xi = 100$ for all $\mu \leq 8.5$ that we consider in this paper. For larger μ also ξ needs to be increased; namely, we use $\xi = 200$ for $\mu = 14.5$, $\xi = 400$ for $\mu = 25.5$, and $\xi = 1000$ for $\mu = 49.5$.

The parameter α determines the location of the section Σ_α. Its choice depends on which aspect of $C^\pm$ is of interest. A natural choice is $\alpha = 0$, such that the folded node (the origin) is contained in Σ_α. This means that C^- and C^+ are computed both up to Σ_0, which emphasizes their intersection curves $C_0^\pm = C^\pm \cap \Sigma_0$. Note that these intersection curves have been computed before by shooting methods (numerical integration of initial values of S^a); see for example, [27, 26, 48]. By contrast, we compute the curves $C_0^\pm$ as well as the surfaces $C^\pm$ themselves with the collocation and continuation routines of the package AUTO [13]. The main advantage of using collocation, as opposed to a shooting method, is that the size of the continuation step is determined as a variation along the entire orbit segment instead of the initial condition alone. This feature is particularly useful for slow-fast systems, which are extremely sensitive to variations in the initial condition [19]. Specifically, we compute the one-dimensional curves $C_0^\pm$ with an adaptation of the software MANBVP [19], where orbit segments are generated according to the local curvature of C_0^-. The two-dimensional surfaces $C^\pm$ are computed with an AUTO run with a fixed continuation step size, which ensures a uniform distribution of mesh points on the surface.

In order to investigate how C^- and C^+ intersect near the folded node at the origin, we consider orbit segments computed up to Σ_α with $\alpha > 0$. By symmetry C^+ ends in $\Sigma_{-\alpha}$, so that the two slow manifolds are seen to interact in the region $-\alpha \leq y \leq \alpha$. To visualize the geometry of this interaction it is convenient to show only the "ribbons" of C^- and C^+ in between the planes $\Sigma_{-\alpha}$ and Σ_α. To this end, we clip each orbit segment of the computed manifold C^- where it intersects $\Sigma_{-\alpha}$. We then determine a mesh with a fixed number of mesh points that are uniformly distributed according to arclength along clipped orbit segments. The resulting ribbons of $C^\pm$ can be readily visualized, which provides insight into the interaction of the slow manifolds; see already Sec. 4.

3.4. Illustration of the method. Figure 2 illustrates our method for the normal form (1.2) with $\mu = 1.2$. Figure 2(a) shows an approximation of the attracting slow manifold C^- for $\alpha = 0$, that is, we computed a collection of orbit segments that start on L_{100}^-, the straight red line in Fig. 2(a), and end in Σ_0, the (x,z)-plane shown in green. The bold red curve in Σ_0 is the intersection C_0^- of C^- with Σ_0, and a small segment of its symmetrical image C_0^+ (blue curve, not labeled) is also shown. We started the continuation from the solution segment (bold black curve) $\gamma_s(tT+t_0)$, $t \in [0,1]$, of the explicitly known strong canard γ_s with t_0 and T as defined in (3.6). The continuation is done in two directions parametrized by the y-coordinate along L_{100}^-, where we start at $y = t_0 < 0$.

Let us first focus on the continuation run where y increases, because this part generates most of the intersection curve C_0^-. Note that it is natural to stop the continuation when $y = 0$ is reached. In practice, we use a user-defined function in AUTO to stop at $y = 0$. (The

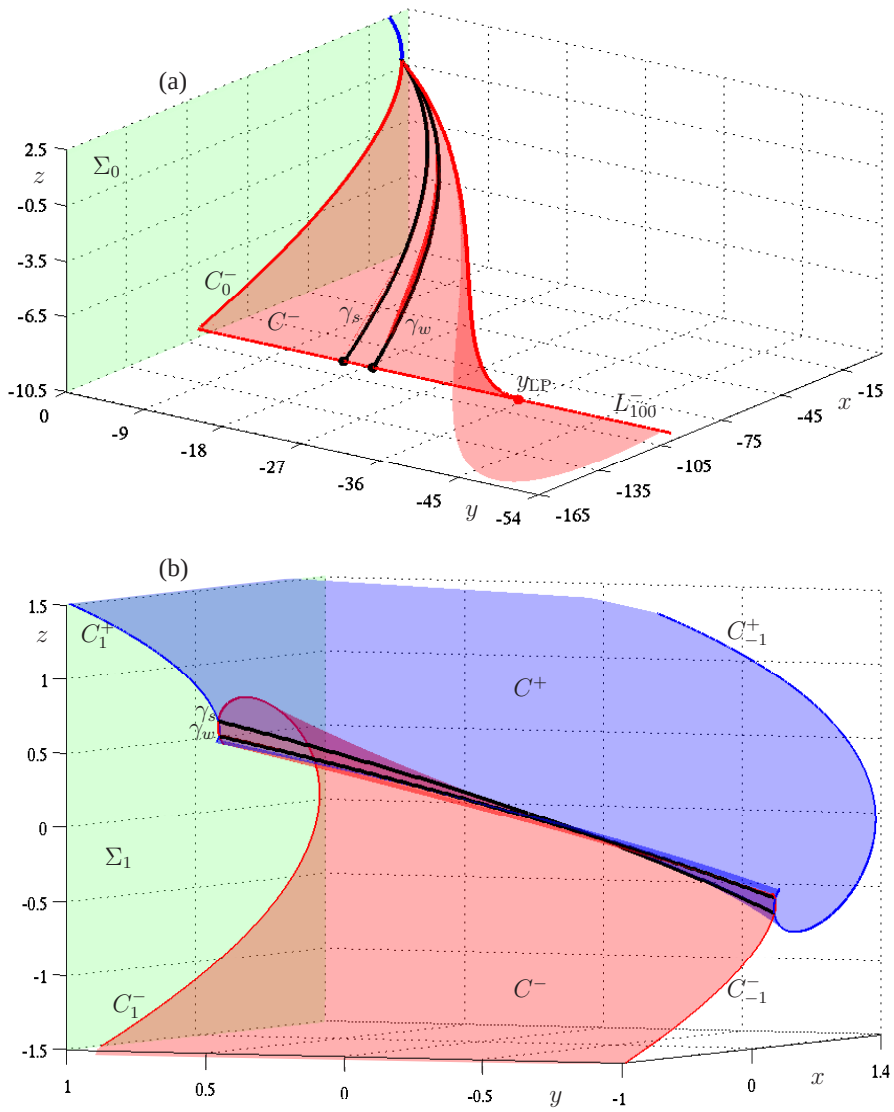

FIG. 2. *Global overview of the slow manifolds for $\mu = 1.2$. Panel (a) shows the attracting slow manifold C^- (red surface) computed from the line of initial conditions L_{100}^- (red line) up to section Σ_0; panel (b) shows the parts of C^- and C^+ (red and blue surfaces, respectively) in between the sections Σ_{-1} and Σ_1. The two primary canards γ_s and γ_w have been hightlighted as bold black curves; the red bold curve (panel (a) only) is the orbit starting at the intersection point $y_{\rm LP}$ between L_{100}^- and the x-nullcline. We also show the intersection curves $C_\alpha^\pm$ of the slow manifolds $C^\pm$ with the sections Σ_0 and $\Sigma_{\pm 1}$. See also the accompanying animation* `dko_fn_a01.gif` *of the computation of C^- for $\mu = 8.5$.*

solution family exists for $y > 0$, but then T becomes negative.) The result from the first continuation run, as shown in Fig. 2(a), is an excellent illustration of Fenichel theory [22], which states that the attracting and repelling sheets of the critical manifold perturb smoothly to locally invariant manifolds for small $\varepsilon \neq 0$ outside a neighborhood of the fold curve F. In fact, outside a neighborhood of the origin, C_0^- is almost identical to the intersection of the critical manifold S with Σ_0. At the scale of Fig. 2(a) it is difficult to see what happens near

the folded node; an enlarged view of $C_0^{\pm}$ is presented in the next section.

During the second continuation run, when y is decreasing, we encounter the orbit segment between L_{100}^- and Σ_0 that corresponds to the weak canard γ_w, for which we have an explicit expression given in (2.12). Note that the symmetry of the normal form forces the attracting and repelling slow manifolds to intersect exactly on the line $z = 0$ in the section Σ_0. Hence, by imposing the user-defined function $\mathbf{u}_z(1) = 0$ as part of the continuation of the one-parameter family that solves (3.1)–(3.2), AUTO [13] automatically detects all canard solutions of the normal form (1.2); a more detailed discussion is provided in Sec. 5. The actual canard solutions are obtained by concatenating the detected orbit segment on C^-, which ends in Σ_0 on the line $z = 0$, with its symmetrical copy on C^+ on the other side of Σ_0.

As y decreases further, we encounter another special solution during the continuation, which is shown as the bold red curve in Fig. 2(a) that starts at the point labeled $y_{\rm LP}$ on L_{100}^-. This point $y_{\rm LP}$ is the unique point

$$y_{\rm LP} = -\frac{2(\mu+1)}{\mu}\sqrt{\xi},$$

where the x-direction of the vector field (1.2) vanishes on L_{100}^-; that is, $y_{\rm LP} \approx 36.777$ is the intersection of L_{100}^- with the x-nullcline for $\mu = 1.2$. We know from Fenichel theory [22] that, away from F, the attracting slow manifold C^- is a graph over the attracting sheet S^a of the critical manifold. Hence, if L_{100}^- were exactly on C^- then all initial conditions on L_{100}^- beyond $y_{\rm LP}$, that is, with y-coordinates less than $y_{\rm LP}$, would lie on (backward-extended) orbit segments that intersect L_{100}^- at y-coordinates larger than $y_{\rm LP}$. This behavior corresponds exactly to the case that an (un)stable manifold in a Poincaré section crosses the locus where the flow is tangent to the section; see [19] for more details.

In practice L_{100}^- only lies approximately on C^- and solutions beyond $y_{\rm LP}$ do not lie exactly on the computed approximation of C^-, but still very close to it. Hence, it appears as though a new part of C^- is obtained, which manifests itself as a very sharp fold, or 'crease,' on the approximation of C^-. From a computational point of view, the continuation makes sense only for $\mathbf{u}(0) \in [0, y_{\rm LP}]$, because continuation beyond $y_{\rm LP}$ produces a second approximation of the same part of C^-. Figure 2(a) does show a computation of C^- past $y_{\rm LP}$ to illustrate what happens. It was reported in [48] that the turning point $y_{\rm LP}$ gives rise to additional canard solutions that persist only for a very short interval of μ-values. The discussion above, however, implies that these additional 'canards' appear due to the numerical error of the approximation and, hence, are spurious. Note further that $y_{\rm LP} \to -\infty$ as $\xi \to \infty$, that is, in the limit where L_ξ^- converges to a line on C^-, the point $y_{\rm LP}$ no longer exists.

Figure 2(b) demonstrated how the ribbons of $C^{\pm}$ in between Σ_1 and Σ_{-1} can be used as a means of visualizing the interaction of the two manifolds. For clarity, the intersection curves $C_1^{\pm}$ and $C_{-1}^{\pm}$ are shown as well. The geometry of $C^{\pm}$ is further enhanced by including the strong and weak canards γ_s and γ_w, respectively.

4. Geometry of the slow manifolds. We now study the slow manifolds $C^{\pm}$ for different values of the parameter μ. We use both $\alpha = 0$ and $\alpha > 0$ in the method from Sec. 3 to illustrate not only the intersection curves $C_0^{\pm}$ of $C^{\pm}$ with Σ_0, as was done in [48], but also the geometry of the two-dimensional slow manifolds $C^{\pm}$ themselves. A main goal is to see how maximal canards arise as new intersection curves between C^- and C^+. In all figures the attracting slow manifold C^- is colored red, the repelling slow manifold C^+ blue, the section Σ_α is green, and the strong canard γ_s and the weak canard γ_w are black. As μ is increased, secondary canards appear, which we label successively as η_i. We adopted a particular color coding for these secondary canards: η_1 is orange, η_2 is magenta, η_3 is cyan, and we repeat these successive colors for each group of three consecutive secondary canards after η_3.

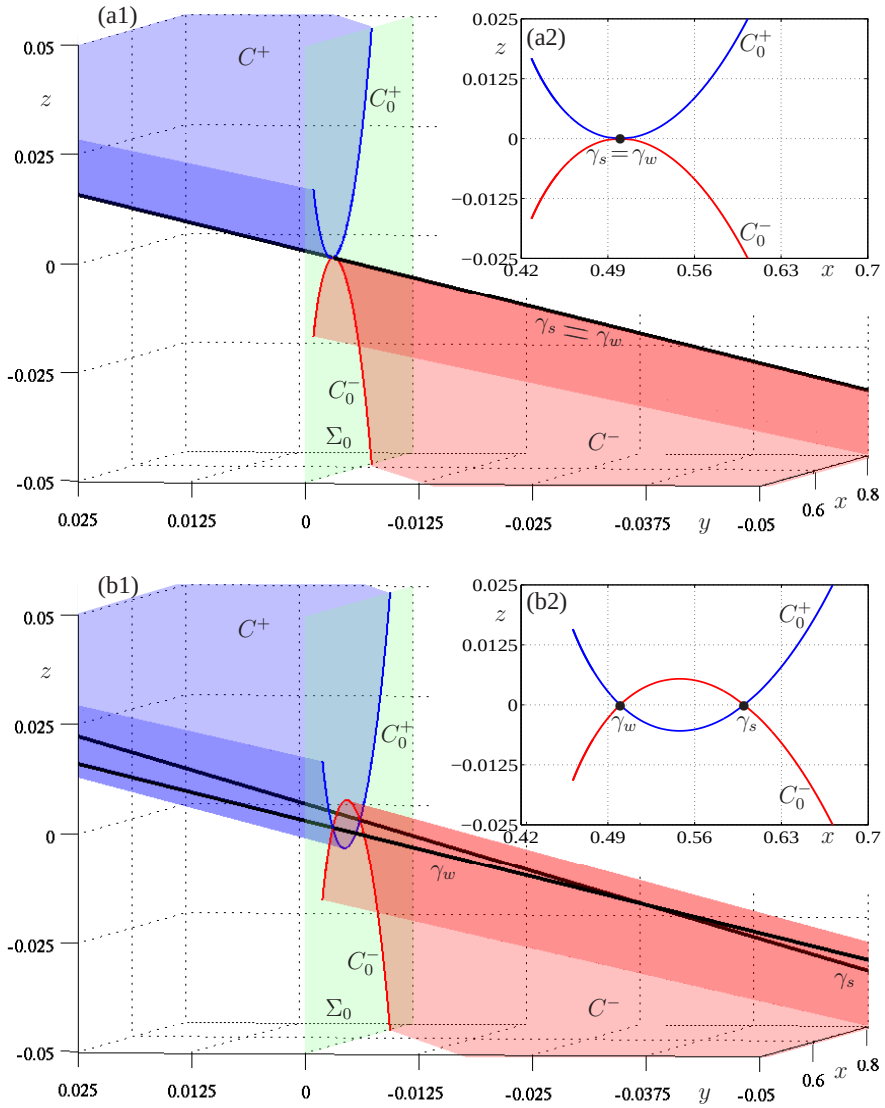

FIG. 3. *Local three-dimensional views of the slow manifolds $C^\pm$ computed up to section Σ_0 (panels (a1) and (b1)), together with two-dimensional illustrations of their intersections $C_0^\pm$ with Σ_0. Panel (a) corresponds to $\mu = 1$ and panel (b) to $\mu = 1.2$. The weak canard γ_w and the strong canard γ_s are shown as black curves and their intersections with Σ_0 are denoted by black dots. See also Figs. 4 and 5.*

4.1. Geometry of $C^\pm$ up to Σ_0. We begin with a series of images for $\mu = 1$, $\mu = 1.2$, $\mu = 2.5$, $\mu = 3.5$, and $\mu = 8.5$ that illustrate the behavior of $C^\pm$ up to the section Σ_0; see Figs. 3(a),(b), 4(a),(b), and 5(a), respectively. Each figure shows a three-dimensional view in a neighborhood of the folded node of C^+ and C^-, computed up to Σ_0, together with the corresponding intersections in the plane Σ_0. To facilitate comparison and analysis, the viewpoint and aspect ratio is identical for all three-dimensional pictures, although the ranges along the axes vary.

Figure 3(a) shows the case $\mu = 1$, which acts as the starting point where $C^\pm$ have a

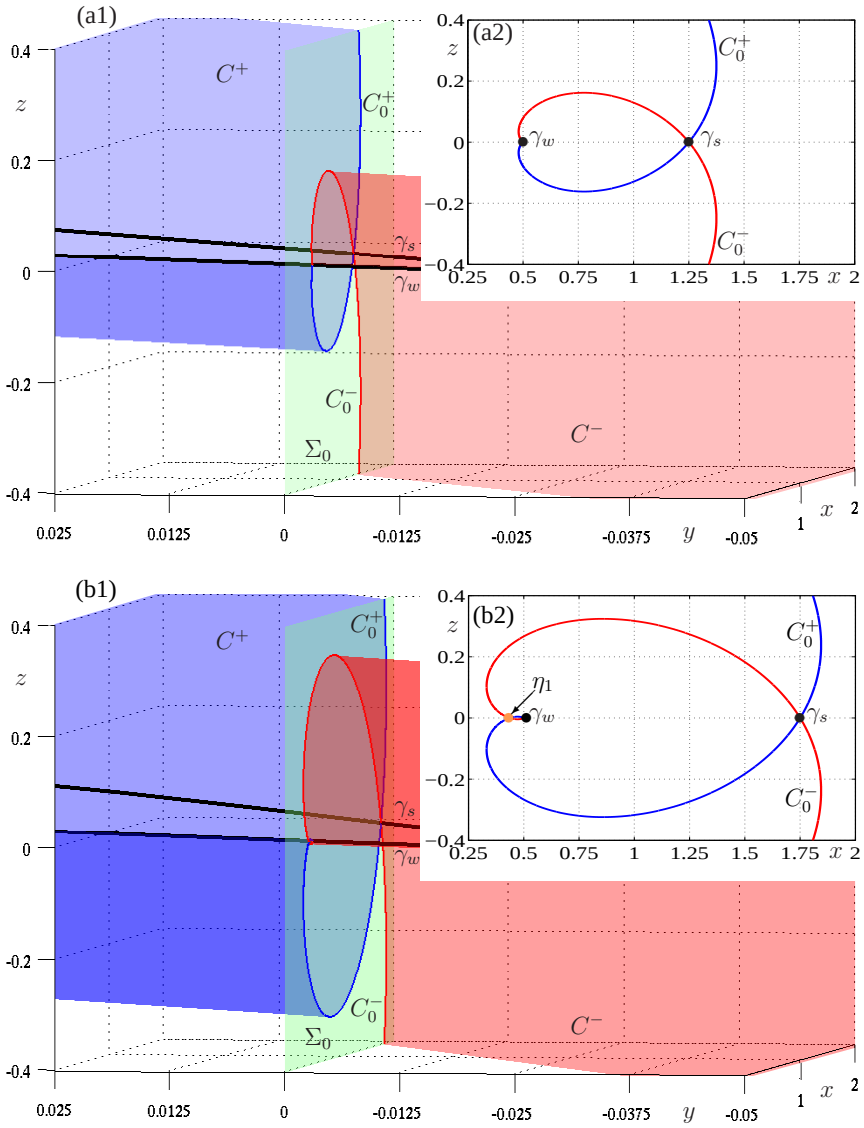

FIG. 4. *Local three-dimensional views of the slow manifolds $C^\pm$ computed up to section Σ_0 (panels (a1) and (b1)), together with two-dimensional illustrations of their intersections $C_0^\pm$ with Σ_0. Panel (a) corresponds to $\mu = 2.5$ and panel (b) to $\mu = 3.5$. Note the existence of the first secondary canard η_1 (orange dot) in panel (b2), which appears in a transcritical bifurcation at $\mu = 3$. See also Figs. 3 and 5.*

non-transverse tangent intersection along a single orbit. The first two (maximal) canards γ_s and γ_w are created as μ is increased. They are shown in Fig. 3(b) for $\mu = 1.2$; see also Fig. 2. Note that γ_s and γ_w are now two distinct orbits of the normal form (1.2) in which the slow manifolds $C^\pm$ intersect transversely. The case $\mu = 1.2$ is representative for all values $1 < \mu < 2$.

A qualitative change occurs at $\mu = 2$. Figure 4(a) shows the situation for $\mu = 2.5$. As can be observed particularly in panel (a2), the tips of $C_0^\pm$ have rotated around so that they now

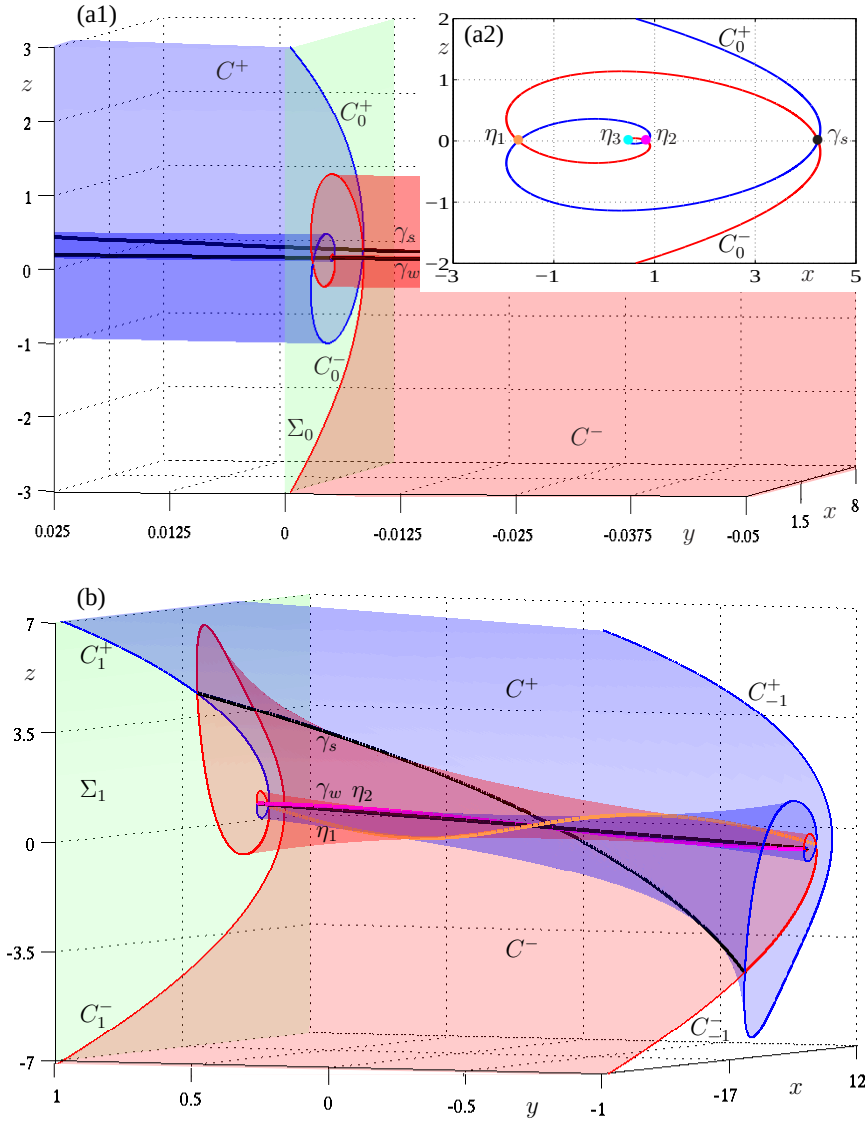

FIG. 5. *Local three-dimensional views of the slow manifolds $C^{\pm}$ for $\mu = 8.5$ computed up to section Σ_0 in panel (a); the inset panel (a2) shows the intersections $C_0^{\pm}$ with Σ_0. See also Figs. 3 and 4 and the accompanying animation* `dko_fn_a02.gif`. *Panel (b) shows the ribbons of $C^{\pm}$ in between Σ_{-1} and Σ_1 along with the corresponding intersection curves $C_{-1}^{\pm}$ and $C_1^{\pm}$. There are three secondary canards η_1, η_2, and η_3, indicated by colored dots in Σ_0 in panel (a2).*

point inside the region delimited by γ_s and γ_w. Indeed, these tips rotate continuously with μ. At $\mu = 2$ the tangent bundles $T_{\gamma_w} C^{\pm}$ coincide and the directions in Σ are parallel to the z-axis, that is, $C_0^{\pm}$ both have a vertical tangency vector at $\gamma_w(0)$ and C_0^- continues smoothly as C_0^+ past $\gamma_w(0)$. For $\mu = 3$ the tips have rotated so that the tangent bundles $T_{\gamma_w} C^{\pm}$ coincide again, but $C_0^{\pm}$ now both have a tangency vector parallel to the x-axis and the manifolds $C^{\pm}$ meet in a cusp. This cusp-shaped tangency is one of the transcritical bifurcations that occur

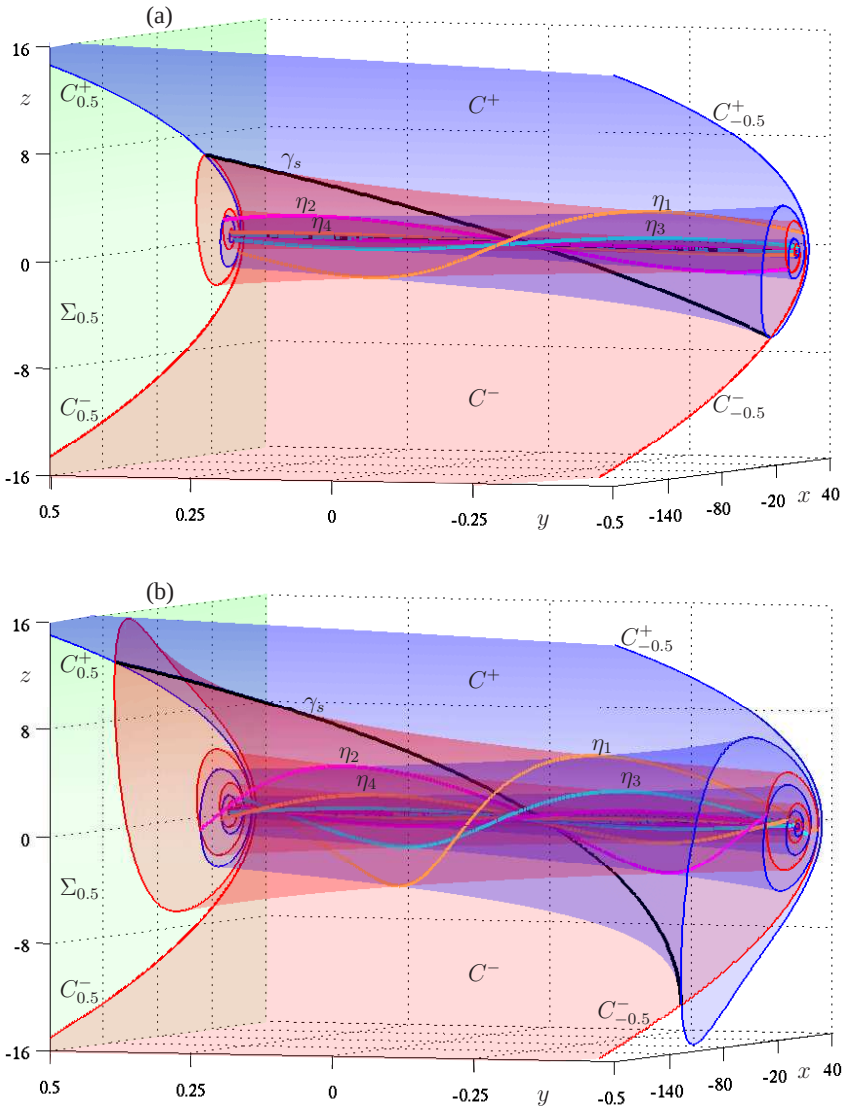

FIG. 6. *Three-dimensional views of the ribbons of $C^{\pm}$ in between $\Sigma_{-0.5}$ and $\Sigma_{0.5}$, together with all maximal canards and the intersection curves $C^{\pm}_{\pm 0.5}$. Panel (a) corresponds to $\mu = 25.5$, with 12 secondary canards, and panel (b) corresponds to $\mu = 49.5$, with 24 secondary canards. See also Figs. 2(a), 5(b) and the accompanying animation* `dko_fn_a03.gif`.

for all odd integer values of $\mu \geq 3$ and results in a secondary canard. Figure 4(b) shows a phase portrait for $\mu = 3.5$ with the first secondary canard η_1 (orange curve). As can be seen clearly in Fig. 4(b2), there are now three intersection points of $C^{\pm}_0$ in Σ_0. Note that γ_w is located between η_1 and γ_s on the x-axis.

Figure 5(a) shows the situation for $\mu = 8.5$, where we have three secondary canards, denoted η_1 (orange), η_2 (magenta), and η_3 (cyan). It gives an idea of how the secondary canards appear as a result of the spiralling motion of $C^{\pm}$ around the weak canard γ_w; this is particularly visible for $C^{\pm}_0$ in Σ_0, shown in Fig. 5(a2) and in the accompanying animation `dko_fn_a02.gif`. The figure also illustrates the fact that $C^{\pm}$ make $\lfloor \frac{\mu-1}{2} \rfloor$ full rotations

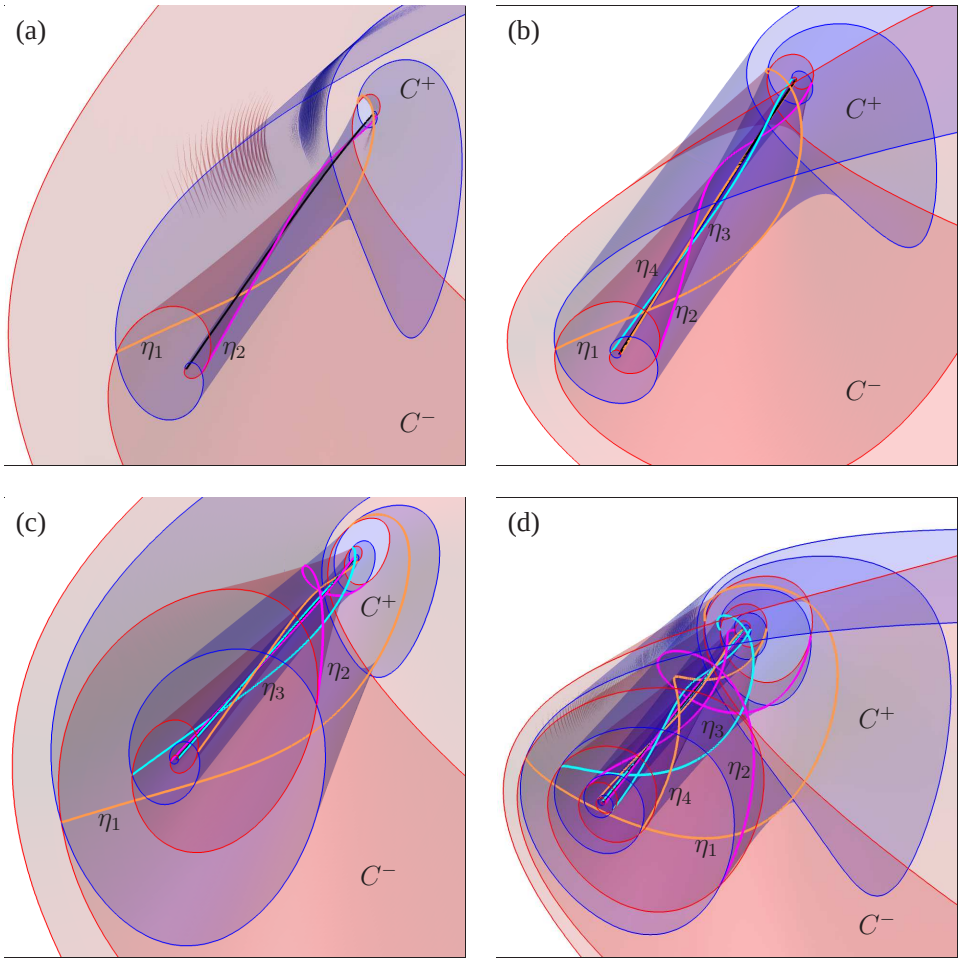

FIG. 7. *Different views of the attracting and repelling slow manifolds C^- and C^+, respectively, to illustrate the spiralling dynamics of the secondary canards around the weak canard γ_w (black curve). The parameter μ is 8.5 in panel (a), $\mu = 14.5$ in panel (b), $\mu = 25.5$ in panel (c), and $\mu = 49.5$ in panel (d).*

around γ_w.

4.2. Ribbons of $C^{\pm}$ near the folded singularity. Figures 3, 4, and 5(a) give a good insight into the topological changes of the geometry of $C^{\pm}$. After the bifurcation of maximal canards at $\mu = 1$, all secondary maximal canards bifurcate from γ_w in transcritical bifurcations at odd integer values of μ. To bring out this behavior more clearly, we also compute ribbons of $C^{\pm}$ in between $\Sigma_{-\alpha}$ and Σ_{α} for suitable $\alpha > 0$. Figure 5(b) shows $C^{\pm}$ in between Σ_{-1} and Σ_1, along with the intersection curves γ_s, γ_w (black curves), η_1 (orange), and η_2 (magenta); note that η_3 is not shown in this picture, because it cannot be distinguished from γ_w at this scale. The intersection curves $C^{\pm}_{-1}$ and $C^{\pm}_1$ in Σ_{-1} and Σ_1, respectively, give some idea of the exponential growth away from the fold curve in forward time (for C^-) and backward time (for C^+) of the solutions on the slow manifolds. Indeed, the maximal canards γ_s, γ_w and η_i, for $i = 1, \ldots, \lfloor \frac{\mu-1}{2} \rfloor$, are the only solutions of (1.2) that grow algebraically both in forward and backward time.

Figure 6 shows $C^{\pm}$ for much larger values of μ, namely, for $\mu = 25.5$ and $\mu = 49.5$ in panels (a) and (b), respectively. Due to the exponential growth of the slow manifolds, we show here ribbons of $C^{\pm}$ only in between $\Sigma_{-0.5}$ and $\Sigma_{0.5}$. The figure shows the increased complexity of $C^{\pm}$ with many more intersection curves that form additional secondary canards. For $\mu = 25.5$ there are twelve secondary canards that wind around γ_w; only the first four are labeled in Fig. 6(a). For $\mu = 49.5$ there are 24 secondary canards, but again only η_1, η_2, η_3, and η_4 are labeled in Fig. 6(b). The increase in μ causes an increase of the spiralling amplitude of the intersection curves $C^{\pm}_{-0.5}$ and $C^{\pm}_{0.5}$ in $\Sigma_{-0.5}$ and $\Sigma_{0.5}$, respectively. By comparing Fig. 6(a) and (b), one can clearly see that the strong canard γ_s and the labeled secondary canards η_1, η_2, η_3, and η_4 lie further away from the weak canard γ_w and from each other; see also the accompanying animation `dko_fn_a03.gif`.

Figure 7 illustrates the increasing complexity with μ of the two slow manifolds near the folded node by showing $C^{\pm}$ for $\mu = 8.5$, $\mu = 14.5$, $\mu = 25.5$ and $\mu = 49.5$. Here we rotated the slow manifolds $C^{\pm}$ about the z-axis with the visualization package GEOMVIEW [39] to generate common enlarged views centered around the weak canard γ_w. In this way, one obtains a good impression of the spiralling behavior of the secondary canards around γ_w and how their positions and distances to γ_w change with μ. Figure 7(a) shows that for $\mu = 8.5$ C^- and C^+ intersect in the two secondary canards η_1 and η_2. For $\mu = 14.5$ there are a total of six secondary canards, four of which, η_1 to η_4, are shown in Fig. 7(b). Note how the distance of η_1 and η_2 from the central weak canard γ_w (black curve) is now much larger for $\mu = 14.5$; in a way, this creates space for η_3 and η_4 to spiral around γ_w as well. For $\mu = 25.5$ there are twelve secondary canards in total, but only η_1 to η_4 are labeled in Fig. 7(c). Similarly, for $\mu = 49.5$ in Fig. 7(d) there are 24 secondary canards, of which the first nine are clearly visible while only η_1 to η_4 are labeled.

5. Geometric study of the secondary canards. As we have seen, the secondary canards arise as intersections of the slow manifolds C^- and C^+. We now find them directly as special orbits within the boundary value problem setup in Sec. 3. This allows us to visualize and discuss their spiralling behavior with respect to the weak canard γ_w. Furthermore, we continue the secondary canards in the parameter μ to reveal an overall bifurcation diagram.

5.1. Detection of secondary canards. During the continuation of (3.1)–(3.2) for fixed μ the end points $\mathbf{u}(1) \in \Sigma_0$ of the computed orbit segments oscillate about the z-axis; see, for example, Fig. 5(a2). Due to symmetry, a secondary canard is characterized by the condition that the z-coordinate $\mathbf{u}_z(1)$ satisfies $\mathbf{u}_z(1) = 0$. Hence, secondary canards can be detected during the continuation by monitoring this condition (with a user-defined function in AUTO). Recall that the point $\mathbf{u}_z(1)$ is a function of the y-coordinate $\mathbf{u}_y(0)$ of its begin point $\mathbf{u}(0)$, which varies along L^-_ξ.

Figure 8 shows the graph of $\mathbf{u}_z(1)$ as a function of $\mathbf{u}_y(0)$ for $\mu = 49.5$, where we show data for the run that starts from the strong canard γ_s for which we have $\mathbf{u}_y(0) = t_0 \approx -1.29$. Due to the spiralling nature of $C^- \cap \Sigma_0$ the graph oscillates with a rapidly decreasing amplitude; note that the continuation is in the direction of negative $\mathbf{u}_y(0)$. The enlargement in the inset of Fig. 8 shows the oscillation of $\mathbf{u}_z(1)$ in the region where η_{12} to η_{15} are detected and the oscillation amplitude has decreased to values of order 10^{-4}. Numerically it becomes increasingly difficult to detect where $\mathbf{u}_z(1)$ changes sign when the oscillation amplitude becomes very small. In other words, for large μ as in Fig. 8 for $\mu = 49.5$ it is quite a challenge to detect the secondary canards that lie very close to γ_w.

For all values of μ in this paper we start the continuation with the AUTO accuracy settings as shown in row (a) of Table 5.1. This is sufficicient for the reliable detection of the η_i even for $\mu = 25.5$, but for the case $\mu = 49.5$ shown in Fig. 8 the detection stops when extrema of $\mathbf{u}_z(1)$ are less than 10^{-9} in modulus. At this stage the secondary canards η_1 to η_{17} have

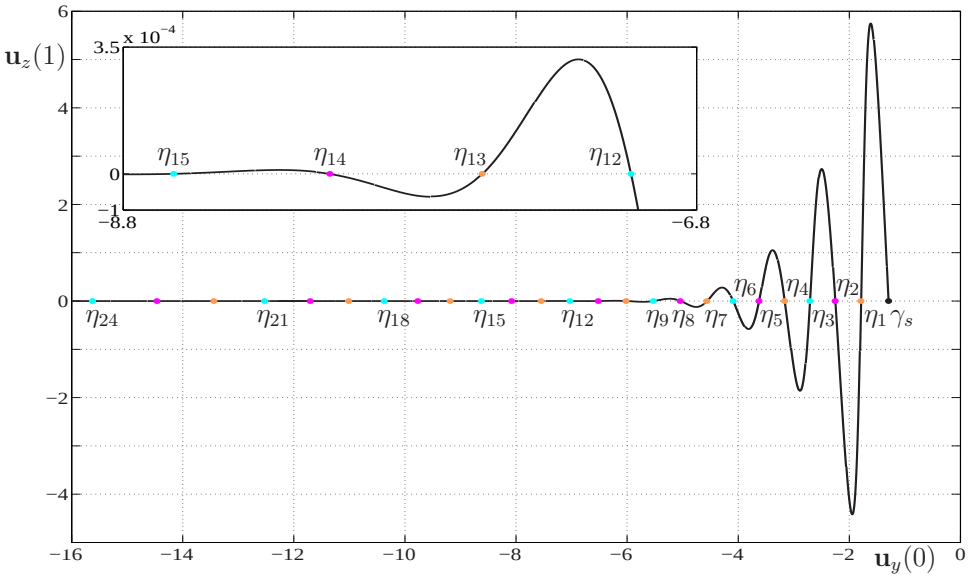

FIG. 8. *Graph of the z-coordinate $\mathbf{u}_z(1)$ of the end point $\mathbf{u}(1)$ of the computed orbit segments on C^- for $\mu = 49.5$ as a function of the y-coordinate $\mathbf{u}_y(0)$ of its begin point $\mathbf{u}(0) \in L_\xi^-$, where we used $\xi = 1000$. The continuation starts from the weak canard γ_w and secondary canards η_i are detected when $\mathbf{u}_z(1) = 0$.*

	NTST	NCOL	DS	DSMIN	DSMAX	EPSS
(a)	200	4	0.001	5×10^{-4}	0.01	10^{-4}
(b)	400	6	0.001	10^{-7}	0.01	10^{-7}

TABLE 5.1

AUTO *accuracy parameters as used during the detecting the secondary canards of* (1.2)*. Row (a) is our regular accuracy setting, and row (b) is the increased accuracy as used for $\mu = 49.5$. Here* NTST *is the number of mesh points,* NCOL *the number of collocation points,* DSMIN *and* DSMAX *are the minimal and maximal stepsizes for the continuation, and* EPSS *is the relative arclength convergence criterion for the detection of special solutions; all other* AUTO *accuracy parameters are set to their default values.*

been detected reliably. The next four secondary canards η_{18} to η_{21} are found in a second run, where we increase the accuracy parameters to the settings given in row (b) of Table 5.1. Nevertheless, the detection of η_{22} to η_{24} is very difficult even with the increased accuracy settings, because $\mathbf{u}_z(1)$ is now consistently below 10^{-15} in modulus. Since we are reaching the limit of machine precision spurious roots of $\mathbf{u}_z(1)$ are reported, out of which we need to select η_{22} to η_{24}. This can be done by taking into consideration the distance between roots in $\mathbf{u}_y(0)$, which leads to a selection that is consistent with the detected secondary canards η_1 to η_{21}; see already Fig. 11(d).

Once a secondary canard has been detected for a fixed value of μ as a zero of $\mathbf{u}_z(1)$, it can be continued in the parameter μ by imposing $\mathbf{u}_z(1) = 0$ as an additional boundary condition. In this way, we can compute the μ-dependent families of all detected secondary canards. We remark here that the oscillations of $\mathbf{u}_z(1)$ near a fixed canard increase as μ is increased. Hence, canards η_i for large i can be detected reliably for larger μ and then continued back into the range of lower values of μ.

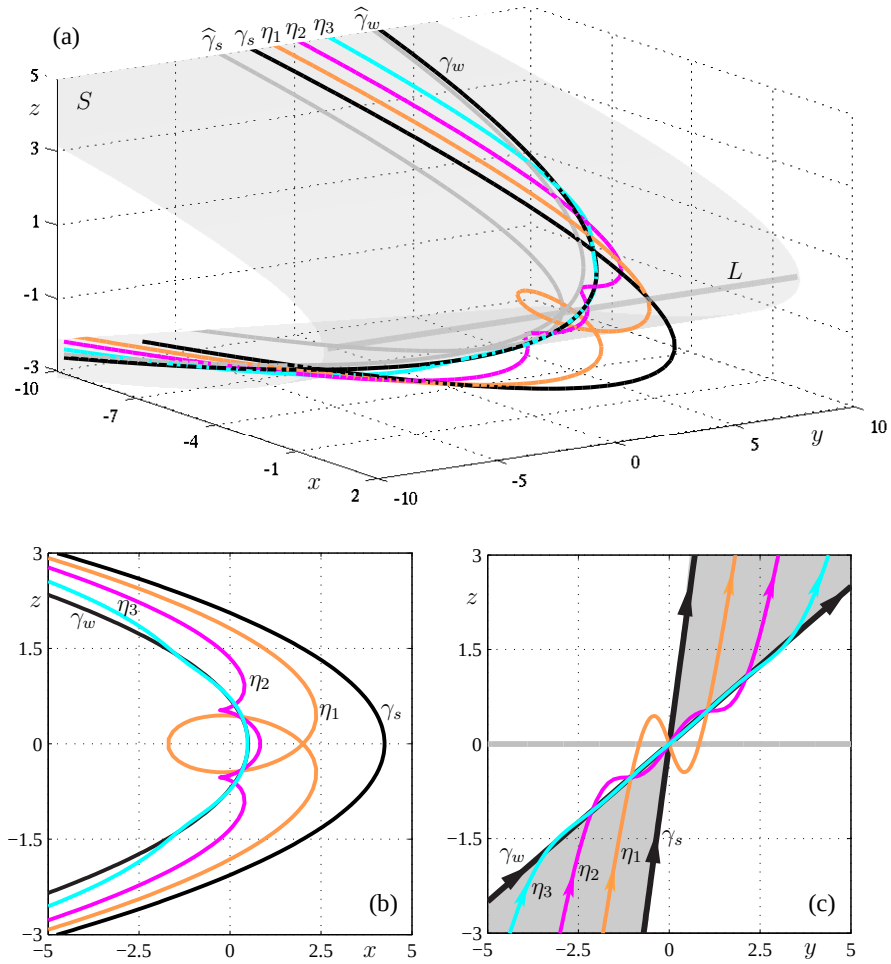

FIG. 9. *Spiralling behavior of the secondary canards of* (1.2) *with* $\mu = 8.5$. *Panel (a) shows a global view of the critical manifold* S *with the fold curve* L *and the singular canards* $\widehat{\gamma}_s$ *and* $\widehat{\gamma}_w$ *(grey). The corresponding strong canard* γ_s *and weak canard* γ_w *of* (1.2) *are shown in black. Note how the three secondary canards* η_1, η_2, *and* η_3 *spiral around* γ_w. *Panels (b) and (c) show the projections onto the* (x, z)- *and* (y, z)-*planes, respectively.*

5.2. Spiralling behavior of the secondary canards. To explain the spiralling of the secondary canards around the weak canard we concentrate on the case $\mu = 8.5$, for which there are three secondary canards, η_1 to η_3. They are shown in Fig. 9 together with the primary canards γ_s and γ_w (black curves). Figure 9(a) is a three-dimensional view of the canards, where we also show for orientation the critical manifold S (the grey parabolic cylinder) with the fold curve L (thick grey line) and the singular canards $\widehat{\gamma}_s$ and $\widehat{\gamma}_w$ (grey) on S. The primary canards γ_s and γ_w (black) are perturbations (on the blown-up sphere) of $\widehat{\gamma}_s$ and $\widehat{\gamma}_w$. Furthermore, the secondary canards η_i lie seemingly parallel to γ_s for $|x|$ large, but follow γ_w near the fold. With increasing i the η_i lie closer to γ_w as they spiral increasingly around it. Figure 9(b) and (c) are projections of the primary and secondary canards onto the (x, z)- and (y, z)-planes, respectively. Figure 9(b) illustrates how each new secondary canard makes one more full rotation around the weak canard γ_w. Figure 9(c) focuses on the (slow) dynamics of

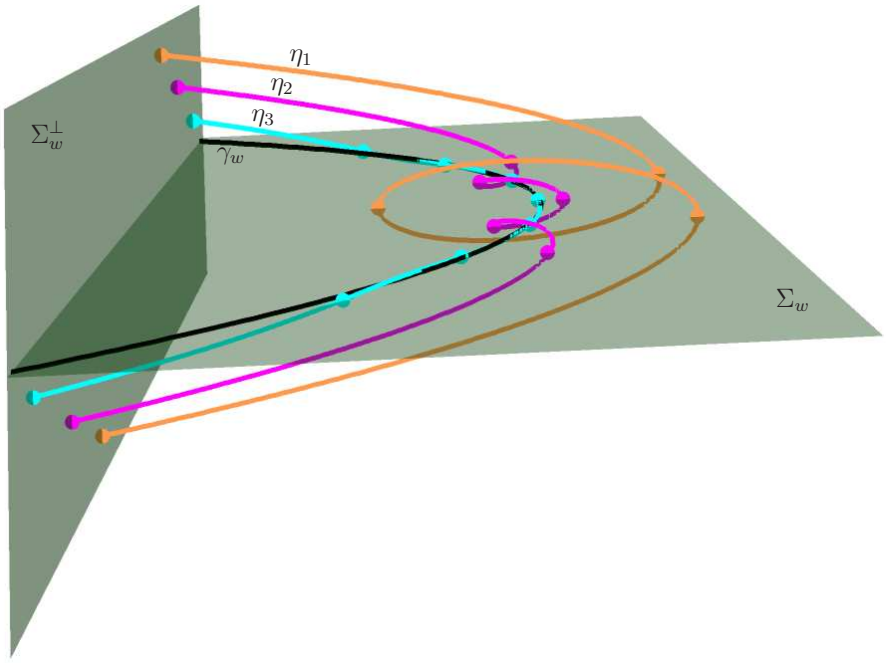

FIG. 10. *Detailed view of the three secondary canards and γ_w for $\mu = 8.5$. The weak canard γ_w lies in the plane Σ_w and the three secondary canards start and end in the plane $\Sigma_w^\perp$ that is chosen perpendicular to Σ_w far enough away from the fold. The intersections of the secondary canards with Σ_w are marked by dots to emphasize the rotations around γ_w.*

the secondary canards in the neighborhood of the fold. The grey regions indicate the funnel through which the weak canards move, which is delimited by the two primary canards γ_w and γ_s; see also Sec. 2.

Figure 10 is a visualization with the package GEOMVIEW [39] in the spirit of a wire and cardboard model to bring out the spiralling of the secondary canards η_1 to η_3 around γ_w. Namely, shown are the plane $\Sigma_w = \{y = 2z\}$ that contains γ_w and the plane $\Sigma_w^\perp = \{x = -10\}$ that is perpendicular to Σ_w chosen so that all spiralling behavior is captured. The secondary canards η_1 to η_3 start on $\Sigma_w^\perp$ below Σ_w and return to $\Sigma_w^\perp$ above Σ_w. Notice that η_1 has three intersection points (yellow dots), η_2 has five intersection points (magenta dots), and η_3 has seven intersection points (blue dots) with Σ_w. This illustrates the theoretical results that η_i makes $\lfloor \frac{\mu-1}{2} \rfloor$ rotations around γ_w. Figure 10 also illustrates that the secondary canards η_i lie successively closer to γ_w in the region of the fold.

The spiralling character of a secondary canard η_i does not depend on the value of μ. When a secondary canards is created in a transcritical bifurcation closest to γ_w at an odd integer value of μ, its rotating property is fixed. This is illustrated in Fig. 11 with projections onto the (y, x)-plane of all canards for $\mu = 8.5$, $\mu = 14.5$, $\mu = 25.5$, and $\mu = 49.5$, respectively. For each case we choose a region of the (y, x)-plane that allows for a comparison between the panels; specifically, the x-maximum of γ_s is fixed and the y-range is adjusted so that the last secondary canard is seen to 'leave' γ_w. Figure 11(a) for $\mu = 8.5$ should be compared directly with Fig. 9. There are six secondary canards in Fig. 11(b), twelve in Fig. 11(c) and 24 in Fig. 11(d). Overall, the secondary canards run parallel to (have the same slope as) the strong canard γ_s for large $|x|$, and then spiral around γ_w. Observe that the

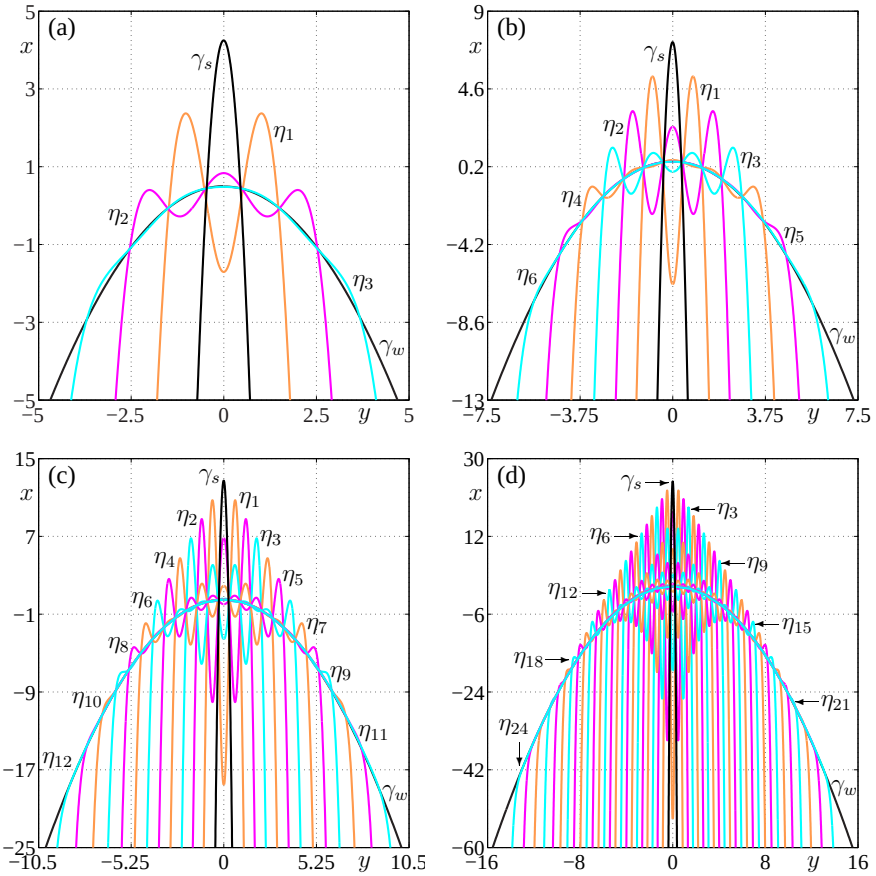

FIG. 11. *Representation in the (y, x)-plane of the primary and secondary canards for four different values of μ. From panel (a) to panel (d) $\mu = 8.5$, $\mu = 14.5$, $\mu = 25.5$, and $\mu = 49.5$, respectively, where shown part of the (y, x)-plan is chosen so that the maximum of γ_s is fixed and all secondary canards are covered.*

maxima of the η_i appear to line up along a curve that connects γ_w to the maximum of γ_s; an initial investigation showed that this curve is not a straight line. It would be an interesting challenge to study limiting features of the canards in a suitably rescaled (y, x)-plane for μ tending to ∞.

5.3. Continuation of the secondary canards in μ. It is a particular advantage of our boundary value problem setup that secondary canards can be continued in the parameter μ. Figure 12 shows the result of the continuation of the secondary canards η_1 to η_{12}, where we plot the x-coordinate $\mathbf{u}_x(1)$ of the end point in Σ_0. Also shown in this bifurcation diagram are the primary canards γ_w and γ_s. They are determined from (2.12) as the straight lines $\mathbf{u}_x(1) = \frac{1}{2}$ and $\mathbf{u}_x(1) = \frac{\mu}{2}$, respectively, which intersect transversely at $\mu = 1$. The continuation was started by detecting all twelve secondary canards for $\mu = 25.5$, where we used $\xi = 1000$ to ensure sufficient accuracy for their continuation for $\mu > 25.5$.

Figure 12(a) shows how η_1 to η_{12} bifurcate from γ_w at odd integer values. Notice that the branches of η_i for odd i are in the region below $\gamma_w = \frac{1}{2}$, while those for even i are in the region above $\gamma_w = \frac{1}{2}$. This agrees with [48, Fig. 17] of Wechselberger, who sketched the

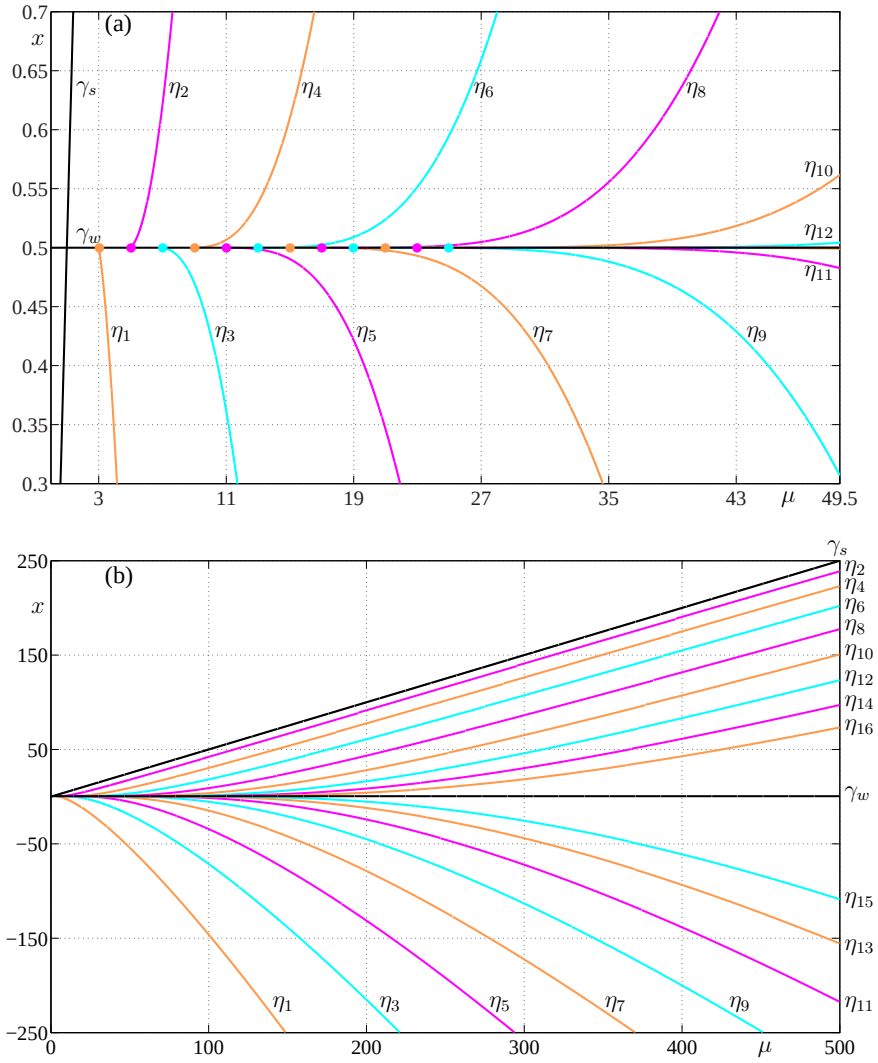

FIG. 12. *Continuation of η_i, $1 \le i \le 12$ in μ. Shown are the projections of η_i onto the (μ, x)-plane with γ_s and γ_w included for reference. Panel (a) is a zoomed view that shows how the first twelve secondary canards bifurcate from γ_w at odd integer values of μ; the bifurcation points for η_1 to $\eta_1 2$ are indicated by thick colored dots. Panel (b) shows an enlarged view of the continuation up to $\mu = 500$.*

branches of secondary canards η_i as straight lines that bifurcate from γ_w at an angle. As can be seen in Fig. 12(a), the branches of η_i are actually tangent to γ_w and the degree of tangency appears to increase with i. Figure 12(b) shows the branches of η_i for the much larger μ-range up to $\mu = 500$. This image suggests that in the limit of large μ the branches for odd i appear to have slope $\frac{1}{2}$ as γ_s, while those for even i appear to have slope $-\frac{1}{2}$. These slopes agree with the slopes suggested by Wechselberger's sketch [48, Fig. 17].

6. Beyond the normal form. It is in the nature of a normal form that (1.2) has special properties. Specifically C^- and C^+ are each other's images under a symmetry operation.

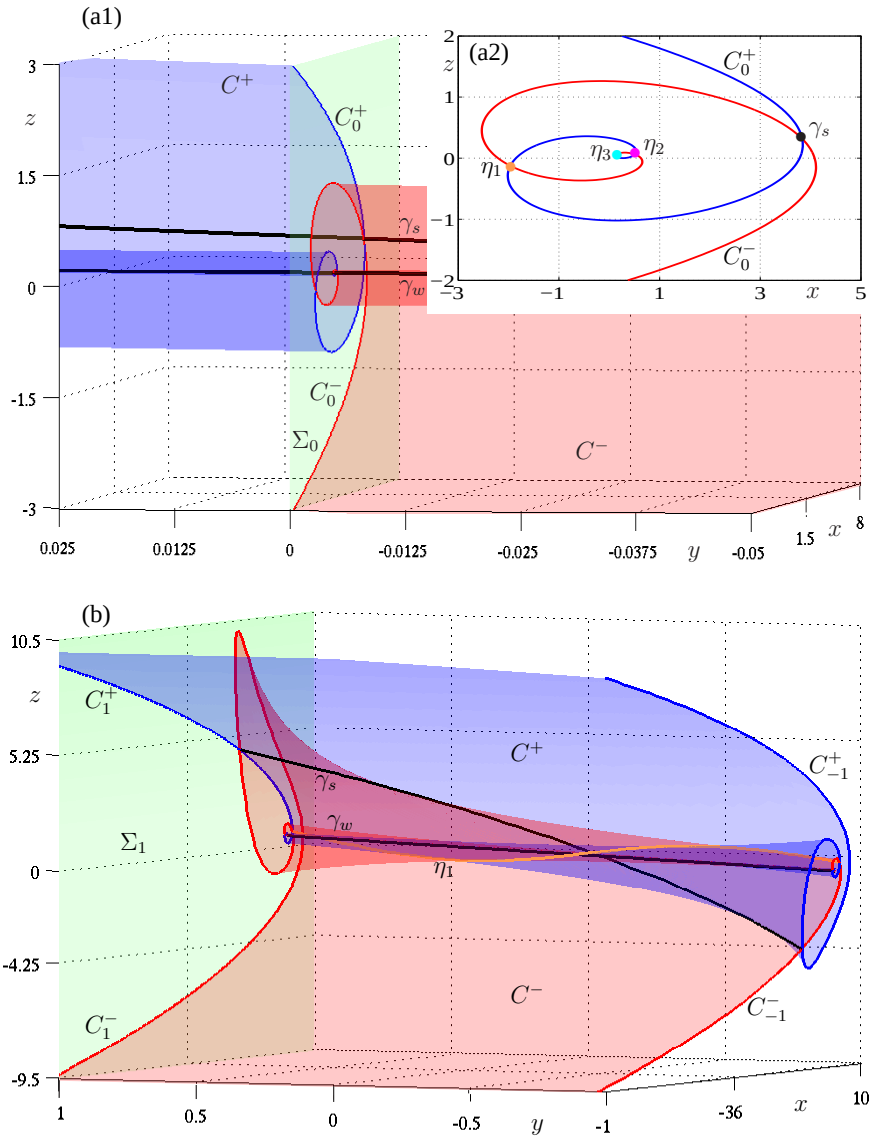

FIG. 13. *Slow manifolds and canard solutions of* (2.9) *with* $\mu = 8.5$ *and* $\varepsilon = 0.1$. *The manifolds are smooth deformations of the equivalent manifolds for* $\varepsilon = 0$, *but the attracting and repelling slow manifolds are no longer related by symmetry; compare with Fig. 5.*

From the computational point of view, this means that only C^- needs to be computed. Furthermore, secondary canards can be detected and continued by considering the condition $\mathbf{u}_z(1) = 0$. However, for a system that is not in normal form the symmetry of the normal form is typically lost. Hence, in general the attracting and repelling slow manifolds must be computed separately as the solution families of two different two-point boundary value problems. As a consequence, the primary and the secondary canards must be detected as solutions correcponding to intersection points of the curves $C^- \cap \Sigma_0$ and $C^+ \cap \Sigma_0$.

As an example, we show here what the slow manifolds look like in the perturbation of

the normal form (1.2) that is given by (2.9) for small nonzero $\rho = \sqrt{\varepsilon}$, that is,

$$\left\{ \begin{array}{rcl} \dot{x} & = & \frac{1}{2}\mu y - (\mu+1)z + \sqrt{\varepsilon}, \\ \dot{y} & = & 1, \\ \dot{z} & = & x + z^2 + \sqrt{\varepsilon}. \end{array} \right. \tag{6.1}$$

Note that system (6.1) has the same critical manifold as the normal form (1.2), so that its slow manifolds can be computed with the same boundary conditions as for (1.2). Namely, we require that the orbit segments start on the line L_ξ^- defined by (3.3). For the computation of the repelling slow manifold, we reverse time in (6.1) and consider

$$L_\xi^+ := \{(-\xi, s, \sqrt{\xi}) \mid s \in \mathbb{R}\},$$

which lies on S^r instead of S^a, again parallel to F at 'distance' $\xi > 0$ from F. Furthermore, we require the orbit segments to end in a transverse section Σ_α given by (3.4) with $\alpha = 0$ or $\alpha = \pm 1$.

We consider here the case $\mu = 8.5$ and $\varepsilon = 0.1$ and fix $\xi = 100$ as before. For $\varepsilon = 0.1$ the explicitly known solution of γ_s of the unperturbed system (1.2) does not work as a starting solution. (Newton's method does not converge.) Therefore, starting from γ_s we first compute the ε-dependent family of orbit segments that solve (6.1) subject to the boundary conditions (3.2). Here we fix the parameter s that defines the position on L_ξ^- to the value (given by γ_s) of

$$s = t_0 = -\sqrt{\frac{2\mu + 4\xi}{\mu^2}}$$

as defined in (3.6). When $\varepsilon = 0.1$ is reached a first orbit segment on C^- has been found; a first orbit segment on C^+ is found similarly by starting a continuation in ε from the part of γ_s that connects L_ξ^+ to Σ_α. We now fix $\varepsilon = 0.1$ and continue in s to sweep out C^- and C^+, respectively.

Figure 13 shows the slow manifolds of (6.1) for $\mu = 8.5$ and $\varepsilon = 0.1$. This figure should be compared with Fig. 5 for $\varepsilon = 0$; for ease of comparison we use the same viewpoints in both figures. In Fig. 13 the slow manifolds C^- and C^+ have deformed and are no longer each other's image under a symmetry operation. Nevertheless, the situation is topologically the same as that for $\varepsilon = 0$ in Fig. 5. Namely, C^- and C^+ intersect in the same way in the primary canards γ_s and γ_w and the secondary canards η_1 to η_3; see Fig. 13(a2) and (b). In particular, the rotating behavior of η_1 to η_3 around γ_w is preserved. The canards are found by detecting orbit segments on C^- and C^+ that end at the same point in Σ_0 (within the accuracy of the computation). Concatenation of the two respective orbit segments results in the representation of the secondary canard as a solution that starts on L_ξ^- and ends at L_ξ^+. After applying a Newton step to get an exact solution to this boundary value problem, detected canards can be continued in a system parameter.

7. Conclusion. We performed a study of slow manifolds and associated canard solutions in a three-dimensional normal form of a slow-fast system with a folded node. Specifically, we computed the two-dimensional attracting and repelling slow manifolds as one-parameter families of orbit segments that satisfy appropriately chosen boundary conditions. This approach also allows us to detect and continue the associated canard solutions in which the two slow manifolds intersect. The visualization of these geometric objects for different values of the normal form parameter μ (the ratio of eigenvalues at the folded node) provided unprecedented insight into the geometry of the dynamics near a folded node. We discussed

in detail how the secondary canards spiral around the weak primary canard and presented the first computed bifurcation diagram showing branches of the secondary canards as a function of μ.

The numerical continuation of solution families of a well-posed boundary value problems can be performed extremely accurately. In our computations we use the continuation and boundary value solver routines of AUTO, which uses pseudo-arclength continuation and collocation with piecewise-polynomial approximations. Hence, the boundary value problems we define are solved subject to established error bounds. Therefore, the accuracy of our calculations of slow manifolds and canard solutions comes down to determining how the choice of boundary condition influences the distance of the approximation from the real object. In our setup we make use of the fact that far away from the fold line the slow manifolds are very close to the critical manifold. Hence, we restrict the approximating orbit segments to such a far away line on the critical manifold. We ensured by numerical checks that the pointwise distance to the true slow manifolds along selected orbit segments is sufficiently small. A more detailed error analysis is a challenging subject for further investigation, because the overall approximation error depends, in general, not only on the distance from the fold curve but also on system parameters.

While this paper concentrates on the normal form of a folded node, our boundary value problem approach to computing slow manifolds and canard solutions can be applied more widely. This was demonstrated with the example of a perturbation of the normal form that breaks the underlying symmetry. In [10] we computed slow manifolds and canard solutions in the self-coupled FitzHugh Nagumo model. This required the implementation of a homotopy approach to generating initial approximate orbits on the attracting and repelling slow manifolds. In this way, we were able to identify sectors between different secondary canards that correspond to mixed-mode oscillations with different numbers of small oscillations.

In the near future we plan to use our computational approach to investigate other slow-fast systems arising in applications, especially those showing mixed-mode oscillations. This is relatively straightforward for the case of three-dimensional vector field models with a clear splitting of the phase space into slow and fast variables, such as the self-coupled FitzHugh Nagumo model [10] or the forced Van der Pol system [6, 28]. However, we believe that the computation of invariant manifolds would also be a very helpful tool in situations where there is no obvious split of the system into slow and fast variables. The goal here would be to identify slow and fast components of the dynamics numerically, and to use this knowledge to unravel the geometry of slow manifolds and associated canard solutions.

REFERENCES

[1] V. I. ARNOL′D, *Singularity Theory*, vol. **53** of London Math. Soc. Lecture Note Ser., Cambridge University Press, Cambridge, 1981.

[2] V. I. ARNOL′D, V. S. AFRAJMOVICH, YU. S. IL′YASHENKO, AND P. L. SHIL′NIKOV, *Dynamical Systems V: Bifurcation Theory and Catastrophe Theory*, Encyclopaedia Math. Sci., Springer-Verlag, Berlin, 1994.

[3] E. BENOÎT, *Systèmes lents-rapides dans* $\mathbb{R}^3$ *et leurs canards*, in Troisième rencontre du Schnepfenried, vol. **109–110** of Astérisque, Soc. Math. France, 1983, pp. 159–191.

[4] E. BENOÎT, *Canards et enlacements*, Inst. Hautes Études Sci. Publ. Math., **72** (1990), pp. 63–91.

[5] E. BENOÎT, J.-L. CALLOT, F. DIENER, AND M. DIENER, *Chasse au canard*, Collect. Math., **31–32** (1981), pp. 37–119.

[6] K. BOLD, C. EDWARDS, J. GUCKENHEIMER, S. GUHARAY, K. HOFFMAN, J. HUBBARD, R. OLIVA, , AND W. WECKESSER, *The forced Van der Pol equation II: canards in the reduced system*, SIAM J. Appl. Dyn. Sys., **2** (2003), pp. 570–608.

[7] M. BRØNS, T.J. KAPER, AND H.G. ROTSTEIN, *Special issue on mixed-mode oscillations*, Chaos, (March 2008).

[8] M. BRØNS, M. KRUPA, AND M. WECHSELBERGER, *Mixed mode oscillations due to the generalized canard*

phenomenon, in Fields Institute Communications, vol. **49**, Amer. Math. Soc., Providence, RI, 2006, pp. 39–63.

[9] F. BUCHHOLTZ, M. DOLNIK, AND I. R. EPSTEIN, *Diffusion-induced instabilities near a canard*, J. Phys. Chem., **99** (1995), pp. 15093–15101.

[10] M. DESROCHES, B. KRAUSKOPF, AND H. M. OSINGA, *Mixed-mode oscillations and slow manifolds in the self-coupled fitzhugh nagumo system*. to appear in Chaos, 2007.

[11] E. J. DOEDEL, *Lecture notes on numerical analysis of nonlinear equations*, in Numerical Continuation Methods for Dynamical Systems: Path following and boundary value problems, B. Krauskopf, H. M. Osinga, and J. Galán-Vioque, eds., Springer-Verlag, New-York, 2007, pp. 1–50.

[12] E. J. DOEDEL, E. FREIRE, E. GAMERIO, AND A. J. RODRÍGUEZ-LUIS, *An analytical and numerical study of a modified van der pol oscillator*, J. Sound Vibr., **256** (2002), pp. 755–771.

[13] E. J. DOEDEL, R. C. PAFFENROTH, A. R. CHAMPNEYS, T. F. FAIRGRIEVE, YU. A. KUZNETSOV, B. E. OLDEMAN, B. SANDSTEDE, AND X. J. WANG, AUTO2000*: Continuation and bifurcation software for ordinary differential equations*. available via `http://cmvl.cs.concordia.ca/`.

[14] M. DOMIJAN, R. MURRAY, AND J. SNEYD, *Dynamical probing of the mechanisms underlying calcium oscillations*, J. Nonlin. Sci., **16** (2006), pp. 483–506.

[15] J. L. A. DUBBELDAM AND B. KRAUSKOPF, *Self-pulsations in lasers with saturable absorber: dynamics and bifurcations*, Opt. Commun., **159**(4–6) (1999), pp. 325–338.

[16] F. DUMORTIER, *Techniques in the theory of local bifurcations: Blow-up, normal forms, nilpotent bifurcations, singular perturbations*, in Bifurcations and Periodic Orbits of Vector Fields, D. Szlomiuk, ed., Kluwer Academic, Dordrecht, 1993, pp. 19–73.

[17] F. DUMORTIER AND R. ROUSSARIE, *Canard cycles and center manifolds*, Mem. Amer. Math. Soc., **121** (1996).

[18] W. ECKHAUS, *Relaxation oscillations including a standard chase on French ducks*, in Asymptotic Analysis II, vol. **958** of Lecture Notes in Math., Springer-Verlag, New-York, 1983, pp. 449–494.

[19] J. P. ENGLAND, B. KRAUSKOPF, AND H. M. OSINGA, *Computing one-dimensional global manifolds of poincaré maps by continuation*, SIAM J. Appl. Dyn. Sys., **4** (2005), pp. 1008–1041.

[20] T. ERNEUX, *Q-switching bifurcation in a laser with saturable absorber*, J. Opt. Soc. Am. B, **5**(5) (1988), pp. 1063–1069.

[21] N. FENICHEL, *Persistence and smoothness of invariant manifolds*, Indiana Univ. Math. J., **21** (1971), pp. 193–226.

[22] ———, *Geometric singular perturbation theory*, J. Differential Equations, **31** (1979), pp. 53–98.

[23] R. FITZHUGH, *Thresholds and plateaus in the hodgkin-huxley nerve equations*, J. Gen. Physiol., **43** (1960), pp. 867–896.

[24] J.-M. GINOUX AND B. ROSSETTO, *Differential geometry and mechanics: applications to chaotic dynamical systems*, Int. J. Bifur. Chaos Appl. Sci. Engrg., **16** (2006), pp. 887–910.

[25] ———, *Slow manifold of a neuronal bursting model*, in Emergent Properties in Natural and Artificial Dynamical Systems, M. A. Aziz-Alaoui and C. Bertelle, eds., Springer-Verlag, New-York, 2006, pp. 119–128.

[26] J. GUCKENHEIMER, *Return maps of folded nodes and folded saddle-nodes*. preprint, 2007.

[27] J. GUCKENHEIMER AND R. HAIDUC, *Canards at folded node*, Mosc. Math. J., **5** (2005), pp. 91–103.

[28] J. GUCKENHEIMER, K. HOFFMAN, , AND W. WECKESSER, *The forced Van der Pol equation I: the slow flow and its bifurcations*, SIAM J. Appl. Dyn. Sys., **2** (2003), pp. 1–35.

[29] M. W. HIRSCH, C. C. PUGH, AND M. SHUB, *Invariant Manifolds*, vol. **583** of Lecture Notes in Math., Springer-Verlag, New-York, 1977.

[30] A. L. HODGKIN AND A. F. HUXLEY, *A quantitative description of membrane current and its application to conduction and excitation in nerve*, J. Physiology, **117** (1952), pp. 500–544.

[31] C. K. R. T. JONES, *Geometric singular perturbation theory*, in Dynamical Systems, C.I.M.E Lectures, Montecatini Terme, June 1994, vol. **1609** of Lecture Notes in Math., Springer-Verlag, New-York, 1995, pp. 44–120.

[32] M. T. M. KOPER, *Bifurcations of mixed-mode oscillations in a three-variable autonomous Van der Pol-duffing model with a cross-shaped phase diagram*, Physica D, **80** (1995), pp. 72–94.

[33] B. KRAUSKOPF AND H. M. OSINGA, *Computing invariant manifolds via the continuation of orbit segments*, in Numerical Continuation Methods for Dynamical Systems: Path following and boundary value problems, B. Krauskopf, H. M. Osinga, and J. Galán-Vioque, eds., Springer-Verlag, New-York, 2007, pp. 117–154.

[34] A. MILIK, P. SZMOLYAN, H. LÖFFELMANN, AND E. GRÖLLER, *Geometry of mixed-mode oscillations in the 3-D autocatalator*, Internat. J. Bifur. Chaos Appl. Sci. Engrg., **8** (1998), pp. 505–519.

[35] E. F. MISHCHENKO, YU. S. KOLESOV, A. YU. KOLESOV, AND N. KH. RHOZOV, *Asymptotic Methods in Singularly Perturbed Systems*, Monogr. Contemp. Math., Consultants Bureau, New-York, 1994.

[36] J. MOEHLIS, *Canards in a surface oxidation reaction*, J. Nonlin. Sci., **12** (2002), pp. 319–345.

[37] J. S. NAGUMO, S. ARIMOTO, AND S. YOSHIZAWA, *An active pulse transmission line simulating nerve axon*, Proc. IRE, **50** (1962), pp. 2061–2070.

[38] V. PETROV, S. K. SCOTT, AND K. SHOWALTER, *Mixed-mode oscillations in chemical systems*, J. Chem. Phys., **97** (1992), pp. 6191–6198.
[39] M. PHILLIPS, S. LEVY, AND T. MUNZNER, *Geomview: an interactive geometry viewer*, Notices Amer. Math. Soc., **40** (1993), pp. 985–988. This software and the accompanying manual are available at `http://www.geomview.org/`.
[40] H. G. ROTSTEIN AND R. KUSKE, *Localized and asynchronous patterns via canards in coupled calcium oscillators*, Physica D, **215** (2006), pp. 46–61.
[41] R. ROUSSARIE, *Techniques in the theory of local bifurcations: cyclicity and desingularisation*, in Bifurcations and Periodic Orbits of Vector Fields, D. Szlomiuk, ed., Kluwer Academic, Dordrecht, 1993, pp. 347–382.
[42] J. RUBIN AND D. TERMAN, *Geometric singular perturbation analysis for neuronal dynamics*, in Handbook of Dynamical Systems, B. Fiedler, ed., vol. 2, Noth-Holland, Amsterdam, 2002, pp. 93–146.
[43] J. RUBIN AND M. WECHSELBERGER, *Giant squid-hidden canard: the 3D geometry of the hodgkin-huxley model*, Biological Cybernetics, **97** (2007), pp. 5–32.
[44] P. SZMOLYAN AND M. WECHSELBERGER, *Canards in* $\mathbb{R}^3$, J. Differential Equations, **177** (2001), pp. 419–453.
[45] ———, *Relaxation oscillations in* $\mathbb{R}^3$, J. Differential Equations, **200** (2004), pp. 69–104.
[46] B. VAN DER POL, *A theory of the amplitude of free and forced triode vibrations*, Radio Review, **1** (1920), pp. 701–710, 754–762.
[47] ———, *On "Relaxation Oscillations" I*, Phil. Mag., **2** (1926), pp. 978–992.
[48] M. WECHSELBERGER, *Existence and bifurcations of canards in* $\mathbb{R}^3$ *in the case of a folded node*, SIAM J. Appl. Dyn. Sys., **4** (2005), pp. 101–139.